Summer 8-10-2021

Bi-Chromatic Microwave Induced Resistance Oscillations on GaAs/AlGaAs Two Dimensional Electron Systems

Kalupahanaliyanage Don Binuka Gunawardana

BI-CHROMATIC MICROWAVE INDUCED RESISTANCE OSCILLATIONS ON GaAs/AlGaAs TWO DIMENSIONAL ELECTRON SYSTEMS

by

KALUPAHANALIYANAGE DON BINUKA HASAN GUNAWARDANA

Under the Direction of Vadym Apalkov, PhD

A Dissertation Submitted in Partial Fulfillment of the Requirements for the Degree of

Doctor of Philosophy

in the College of Arts and Sciences

Georgia State University

2021

ABSTRACT

Illuminating high mobility GaAs/AlGaAs samples with microwaves has revealed interesting radiation and matter coupling properties. Many studies have been carried out to perceive the microwave-induced oscillatory behavior in diagonal resistance of GaAs/AlGaAs 2D electron systems placed in an external magnetic field. Bichromatic Microwave excitation of high mobility 2D electron systems provides an extra tool to identify the physical mechanisms behind the microwave-induced zero resistance states. Here, we study the oscillatory behavior of diagonal resistance as a function of magnetic field under dual radiation excitement when the system is illuminated with microwave radiation with two different frequencies. The behavior of diagonal resistance is analyzed both experimentally and theoretically. We have photo-excited the GaAs/AlGaAs Hall bar high mobility sample at cryogenic temperatures with microwave radiation at two frequencies with different combinations of high and low frequencies. The intensities of microwave radiation from both sources have been also systematically changed to study their effect on the Microwave induce magnetoresistance behavior. To enhance the sensitivity of experimental results, a technique using two Lock-in amplifiers was implemented to extract the derivative of the diagonal magnetoresistance. Our theoretical simulations were based on the radiation-driven electron orbit model. The main outcome of our research is that for bichromatic microwave excitations, the induced oscillatory behavior of magnetoresistance at low magnetic field is determined by lower-frequency microwave radiation, while at large magnetic field, the magnetoresistance is mainly affected by the higher-frequency component. Our theoretical simulations have supported this experimental observation.

INDEX WORDS: Mobility, 2D electron systems, Zero Resistance States, Microwave induced oscillatory behavior in diagonal resistance, magnetoresistance, Radiation driven electron orbital model, Diagonal resistance

BI-CHROMATIC MICROWAVE INDUCED RESISTANCE OSCILLATIONS ON GaAs/AlGaAs TWO DIMENSIONAL ELECTRON SYSTEMS

by

KALUPAHANALIYANAGE DON BINUKA HASAN GUNAWARDANA

Committee Chair: Vadym Apalkov

Committee: Unil Perera

Russel White

Sidong Lei

Electronic Version Approved:

Office of Graduate Studies

College of Arts and Sciences

Georgia State University

August 2021

DEDICATION

To all who supported and given opportunity .

ACKNOWLEDGEMENTS

I would like to thank my current advisor, Dr. Vadym Apalkov, for his guidance and support towards the completion of this project. I thank my previous supervisor, Dr. Ramesh Mani, for his guidance towards all the experimental and calculated results obtained for this thesis. Moreover, I also like to thank all my committee members for their support and kind understanding. In addition, I am also grateful to all the funding agencies for supporting this project. The U.S. Department of Energy, Office of Basic Energy Sciences, Material Sciences, and Engineering division under the Grant No. DE-SC0001762 has funded magnetotransport studies at Georgia State University. Army Research Office has funded microwave/millimeter/terahertz study under the Grant No. W911NF-14-2-0076 and W911NF-15-1-0433. Additionally, I would like to thank all the people at the workshop for their expertise and support. Finally, I would like to thank my past and present group members for their support, encouragement, and helping me to overcome hard times.

TABLE OF CONTENTS

LIST OF FIGURES

LIST OF ABBREVIATIONS

- 2D – 2 Dimensional
- 2DES – 2 Dimensional electron system
- bMIMO – Bichromatic microwave-induced magneto resistant oscillation
- DOS – Density of states
- FQHE – Fractional Quantum Hall Effect
- IQHE – Integer Quantum Hall Effect
- LHe4 – Liquid Helium 4
- LL – Landau Level
- MBE – Molecular Beam Epitaxy
- MIMO – Microwave induced magneto resistant oscillation
- MOSFET – Metal Oxide Semiconductor Field Effect Transistor
- MW – Microwave
- QHE – Quantum Hall Effect
- SdH – Shubnikov de Hass oscillations
- WL – Weak localization
- ZRS – Zero Resistance State

1 INTRODUCTION

1.1 Purpose of the Study

Low dimensional electron systems have been thoroughly studied in the last decade due to the peculiar and, in most cases, enhanced electronic characteristics they exhibit. Regarding two-dimensional electron systems(2DESs), GaAs/AlGaAs heterostructures are extremely useful in many areas, including quantum hall physics, high mobility transport systems, quantum computation, etc. A better understanding of those low-dimensional structures would enable better device performance and the applications it could be used.

The purpose of this study is to explore the low-temperature electrical transport characteristics of high mobility GaAs/AlGaAs 2DES subjected to a perpendicular magnetic field under bichromatic Microwave (MW) irradiation. Further, this dissertation is designed to provide an insight into the bichromatic Microwave Induced Magnetoresistant Oscillation (bMIMO) line shape evolution under parameters such as Microwave power, magnetic field, etc. The experimental and calculated results (except for figures 3.14 and 4.5) in this thesis were obtained in Prof. R. G. Mani's group at Georgia State University under Dr. Mani’s guidance. As for the next part, bMIMO was simulated using a semiclassical model developed to explain monochromatic Microwave Induced Magnetoresistant Oscillation behavior by J. Inarrea et al. [3]

1.2 Dissertation structure

This dissertation consists of 5 chapters. Here a brief introduction of GaAs/AlGaAs heterostructures and the 2DES fabricated using the band bending of those two materials are explained. Chapter 2 introduces the pathway for Microwave Induced Magnetoresistant Oscillations (MIMOs), starting from the classical hall effect and following through quantum

effects observed in 2DESs in this research area. A study on theoretical models developed to explain the behavior of 2DES at the MIMOs region is also presented.

Chapter 3 mainly focuses on the experimental setup and the experiment itself. Here the techniques and the equipment setup used to observe MIMOs and bMIMOs using GaAs/AlGaAs 2DES at cryogenic temperatures $\sim 1.7K$ is explained. The bMIMO line shape evolution with the Microwave powers and the bMIMO dependency with the magnetic field will be analyzed using the experimental diagonal resistance of the sample and half-cycle plots. Also, the difficulty of observing MIMO and bMIMO at low magnetic fields was overcome by using a two Lockin amplifier technique to observe the derivative of diagonal resistance. Inspired by the transition time of photoexcited electrons, a qualitative model associated with Landau level (LL) separation was developed to explain the bMIMO lineshape evolution with the magnetic field.

Chapter 4 describes the radiation-driven orbit model suggested by Inarrea et al. and the modification to simulate the dual radiation excitation. Here we present the modified model's data, which exhibits a similar lineshape pattern as the experimental data. MW power of the MW radiation used was changed systematically, and the changes in the diagonal resistance with respect to the inverse magnetic field were simulated. Although some differences in the experiment and simulated results could be seen, the line shapes of both results show similar characteristics with the change of MW power, and the magnetic field applied.

Chapter 5 summarizes our result of both the experimental and theoretical parts. Also, further improvements that can be done is discussed in this chapter.

2 GAAS/ALGAAS 2D ELECTRON SYSTEMS

After the innervation of diodes and transistors' from semiconductor materials, the next goal was to build better and more efficient devices that use a smaller space. In1965, Gordon Moore, the co-founder of Intel, introduced Moore's law[12], which exhibits the semiconductor industry trend for coming years as that the number of transistors per square inch doubled every year. Later it was found out that when the semiconductor's size decreases, the surface to volume ratio also increases dramatically, which gives rise to Nano-technology(Nano effects). Here, in this region, materials start to exhibit otherwise unseen quantum phenomena. Like many characteristics of the semiconductor, electron transport is also highly affected by the shrinkage of the material size. Confinement of electrons in areas comparable to the de Broglie wavelength of electrons causes quantum size effects and electron energy quantization[13]. Such confinement could trap the electron motion along one of the dimensions giving rise to a 2D electron system, which flows freely in the other two dimensions.

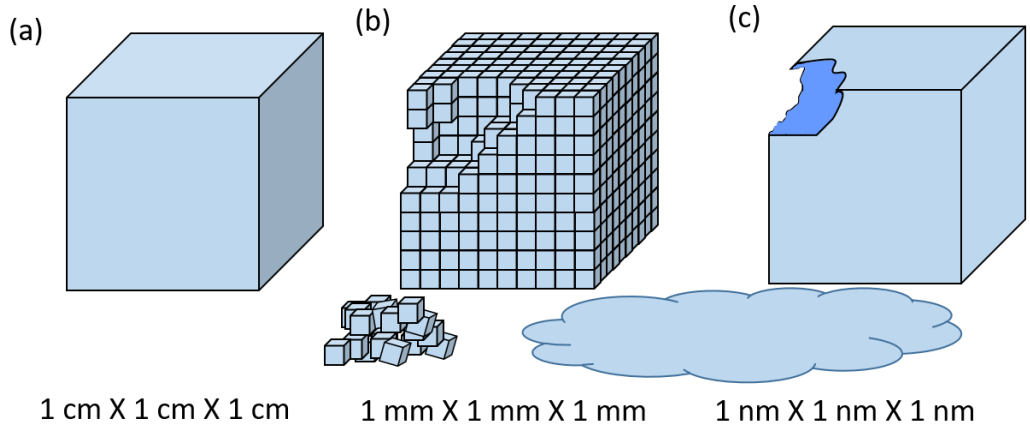

Figure 2.1 Illustration of increment of the surface area provided from Nanomaterial. (a) $1\ cm^3$ *Solid cube with a side length of* $1\ cm$ *with a total area of* $6\ cm^2$*, (b) the same volume covered with cubes with side length* $1\ mm$ *with the total surface area of* $60\ cm^2$*, (c) the same volume covered with cubes with side length* $1\ nm$ *with the total surface area of* $6 \times 10^7\ cm^2$*. Surface:Volume ratio rapidly increases while reducing the sample size emerging quantum effects of the material.*

2.1 2D electron systems

Formerly scientists have fabricated 2DESs based on n-channels Si metal oxide, known as Si – MOSFETs[14], where the electrons were confined in the interface of Si/SiO_2. 2DESs could also be formed in many different manners, for instance, on top of liquid helium surfaces[15], where electrons tend to attach to surface helium molecules. 2DES could be formed using topological insulators. Another alternative uses 2D materials like graphene[16], limiting the electron motion in one direction geometrically. Here, in this study, we focus on 2DES obtained from GaAs/AlGaAs heterostructure [17].

As mentioned before, 2DES attract so much attention due to the quantum mechanical phenomena we would observe using them. For the electron energy in a 2DES trapped in a square well with a side length of 'a' with an infinite potential well along z-direction could be written as,

$$E_N = \frac{\pi^2 \hbar^2 N^2}{2m^* a^2} \ . \tag{2.1}$$

Energies of the electrons are no longer continuous but discreet depending on the quantum number N and effective mass of electrons in the material m^* [13, 14]. GaAs/AlGaAs heterostructure forms a non-rectangular potential well with a finite depth, whose energy could be approximated as,

$$E_N \sim \frac{\hbar^2 N^2}{m^* a^2} \ . \tag{2.2}$$

Since the electrons are confined in z direction and are free to move in xy plane, the total size quantized energy of the electrons could be written using electron's momentum along x and y direction as p_x and p_y respectively.

$$E_{Total} = E_N + \frac{\left(p_x^2 + p_y^2\right)}{2m^*} . \tag{2.3}$$

For the electrons to be trapped in particular energy levels for the sample to exhibit size quantized effects the electron energy separation, $(E_{N+1} - E_N)$ should be higher than the thermal energy, kT of the system, i.e. $(E_{N+1} - E_N) \gg kT$. This suggests that the lower the temperature is needed for better observations of size-quantized effects.

Also, the uncertainty of energy, ΔE should be lower than the electron energy levels to consider a discreet energy spectrum $(E_{N+1} - E_N) \gg \Delta E$. Here, the uncertainty in energy could be written as, $\Delta E = \hbar/\tau$, where τ is the transport scattering time. The transport scattering time could be written in terms of mobility (μ) because $\tau = m^*\mu/e$. So higher the mobility, the lower the uncertainty in energy. To obtain discreet electron energy levels to observe size-dependent quantum phenomena in those 2DESs high mobility samples is critical.

2.2 GaAs/AlGaAs Heterostructure

High-quality, low defect materials with high mobility are essential to study the quantum effects of 2DES. Molecular Beam Epitaxy (MBE) is a growth technique that allows semiconductor material growth on top of each other yielding high quality and atomically flat surfaces. This study is about GaAs/AlGaAs heterostructure with two different band energies $E_g(GaAs)$ and $E_g(AlGaAs)$ [18]. The different conduction band energy levels in two materials form a triangular quantum well in the interface due to band bending, which is used to trap electrons confined in z directions as shown in figure 2.2, allowing electrons to move freely only two-dimensionally. That confined electron system is called a 2D electron gas.

Likewise, all the other materials, the formed 2DES at the GaAs/AlGaAs junction, suffer the problem of scattering from ionizing impurities, interface roughness, etc. MBE growth advancement allows scientists to achieve low surface roughness [14, 17, 18]. Low enough cryogenic temperatures below 4.2 K could eliminate phonon scattering which could be achieved

by liquid Helium-4 (LHe4) and Helium-3 or mixture of those. As shown in figure 2.2 the introduction of a spacer layer between two semiconductor materials suppresses the ionized impurity scattering [19]. This method is known as modulation doping or remote δ doping. All those methods combined could result in GaAs/AlGaAs heterostructure with very high mobility in the order of $\sim \times 10^7\ cm^2V^{-1}s^{-1}$ at liquid helium temperatures.

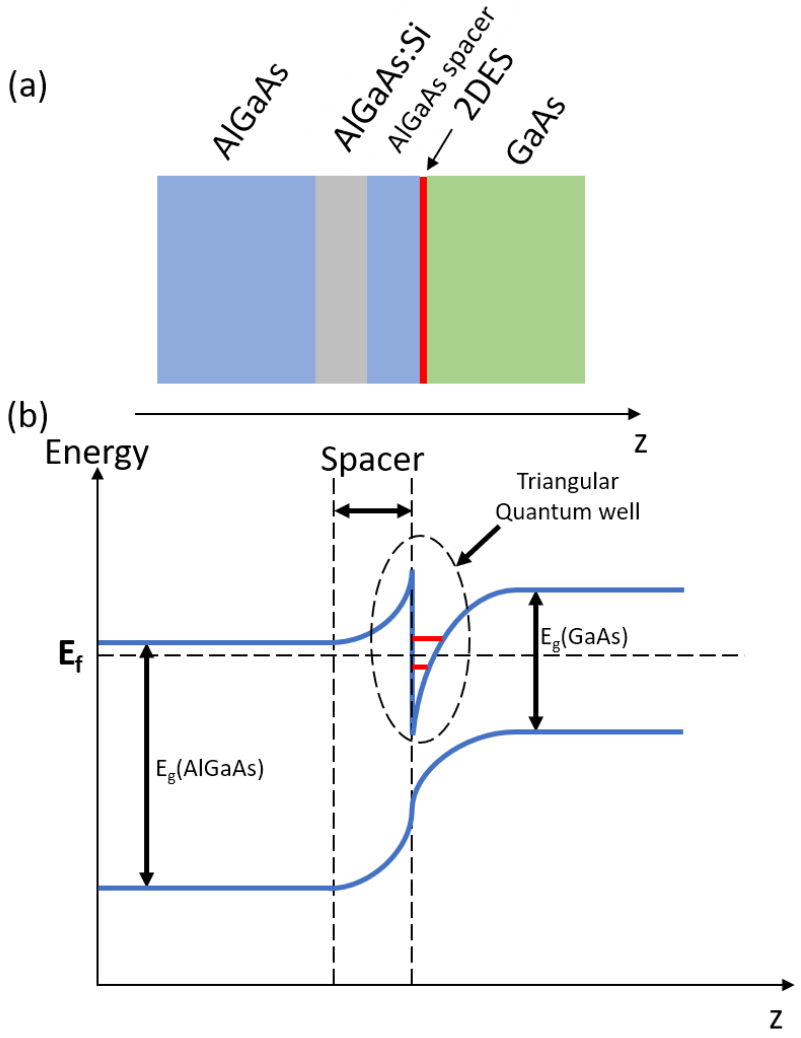

Figure 2.2 Schematic of the GaAs/AlGaAs heterostructure with energy band diagram. (a) GaAs/AlGaAs heterostructure schematics. (b) Energy band diagram of GaAs/AlGaAs heterostructure. Electrons provided by the AlGaAs:Si layer travel through the AlGaAS spacer layer to the conduction band region of GaAs due to adjustment in fermi energy of the system where electrons get trapped inside the triangular quantum well formed due to band bending the interface. Trapped electrons' motion is restricted in z direction, making it a 2DES.

2.3 Landau Levels

Electrons subjected to a perpendicular magnetic field follow a circular path due to the Lorentz force acting on them. Quantization of those cyclotron orbits of charged particles is known as Landau quantization. Here, we consider a 2DES in xy plane subjected to a perpendicular magnetic field in z direction. The quantized energy levels using the Eigenvalues of a spinless electron yield and energy spectrum as

$$E_n = \hbar\omega_c\left(\frac{1}{2} + n\right). \tag{2.4}$$

where n is an integer corresponding to the landau energy level [13] and $\omega_c = eB/m^*$ is the cyclotron frequency. The discreet energy levels relate with $n = 0,1,2,3,$ ... are known as Landau Levels (LLs). Thus, using equation (2.2) and (2.4) the total energy for a spinless electron could be written as,

$$E = E_N + \hbar\omega_c\left(\frac{1}{2} + n\right). \tag{2.5}$$

By taking Zeeman splitting of the LLs, the total energy for the carriers in the 2D plane could be written as

$$E = E_N + \hbar\omega_c\left(\frac{1}{2} + n\right) \pm \frac{1}{2}\mu_B g B\,. \tag{2.6}$$

where g is the electron g-factor and μ_B is the Bohr Magneton. The " + " and "− " signs represent the spin up and down electrons, respectively. The Fermi energy could be written using the Fermi wave vector k_F as,

$$E_F = \frac{\hbar^2 k_F^2}{2m^*}. \tag{2.7}$$

At sufficiently low temperatures, typically, the energy separation of the 2DES is considerably more significant than the Fermi energy. And we could consider that due to the low energy in the system,

only the energy level corresponding to $N = 1$ is occupied. So the energy values only depend only on the quantum number n and the spin direction. The LLs highly degenerate, which depends on the 2DES sample size in xy plane. The size of an electron orbit, also known as the magnetic length, l_B is given by

$$l_B = \sqrt{\frac{\hbar}{eB}}. \tag{2.8}$$

Then since each LL occupies an area of $2\pi l_B^2$ the density of states, n_{DS} for a given LL could be written as,

$$n_{DS} = \frac{eB}{h}. \tag{2.9}$$

A magnetic flux quantum [20] is defined as $\phi = h/e$ so that one electron occypies an area of a single flux quantum. Here, we could define number of filled LLs as filling factor ν, which could be written as

$$\nu = \frac{n_e}{n_{DS}} = \frac{n_e h}{eB} = \frac{n_e\, \phi}{B}. \tag{2.10}$$

Here, n_e is the density of charge carriers. LLs are well quantized in an ideal case, as shown in figure 2-3(b). Still, in practice, electrons moving in a positive lattice have many defects, leading to LL broadening, as shown in figure 2-3(c), creating two electrons states called extended and localized states. LL width of those systems is given by,

$$\Gamma = p\sqrt{\frac{B}{\mu}}. \tag{2.11}$$

Here, μ is the mobility and $p = 2.3 \pm 0.3\ meV\ T^{-1}$. If the sample is a high-quality sample, then $\Gamma \ll \hbar\omega_c$. Figure 2-3 [21] shows the formation of LLs of a 2DES subjected to a perpendicular magnetic field.

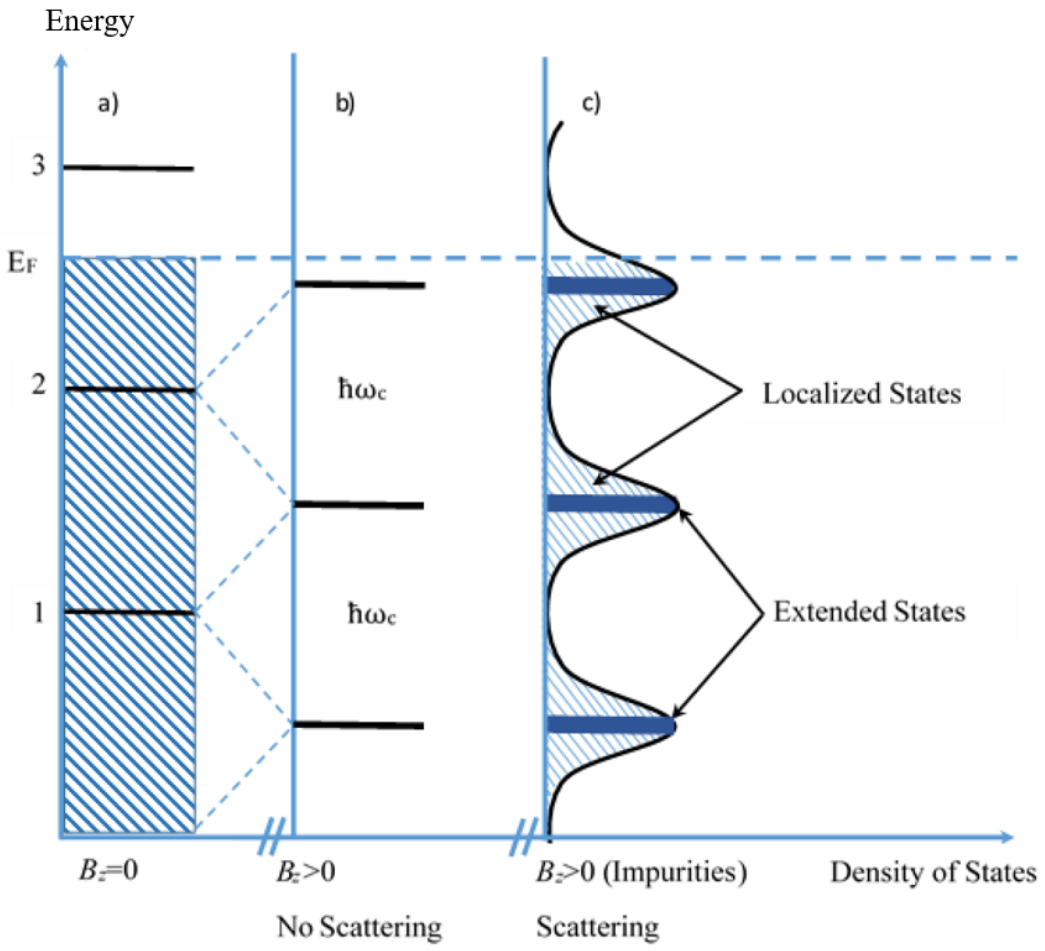

Figure 2.3 Formation of LLs in a 2DES subjected to a perpendicular magnetic field. (a) When $B_z = 0$ the electrons are filled up to the Fermi energy level of the system. (b) In the ideal situation without any impurities in the sample, the introduction of a magnetic field $B_z > 0$ separates the continuous energy spectrum into discreet LLs with energy separation $\hbar\omega_c$. (c) The impurities in the sample broaden the LLs into extended stated (dark blue regions) and localized states (stripped light blue regions). E_F indicates the Fermi energy level of the system. At cryogenic temperatures, localized states do not conduct current while the extended states support conduction[11].

2.4 Hall Measurements from Druid Model

Consider a 2DES confined in z direction and free in xy plane with velocity, $\vec{v} = (\dot{x}, \dot{y}, 0)$. If the system is subjected to a magnetic field $\vec{B} = (0,0,B_z)$, an electric field $\vec{E}$ the using Lorentz formula equation of motion of the electrons could be written as with a constant scattering relaxation time τ as

$$m\frac{d\vec{v}}{dt} = -e\vec{E} - e\vec{v} \times \vec{B} - \frac{m\vec{v}}{\tau}. \tag{2.12}$$

This is the most straightforward equation of motion for charge transport using kinetic theory for gases, known as the Drude model [14]. For the stationary solution when $d\vec{v}/dt = 0$,

$$\vec{v} + \frac{e\tau}{m}\vec{v} \times \vec{B} = -\frac{e\tau}{m}\vec{E}. \tag{2.13}$$

Using the current density $\vec{J} = -ne\vec{v}$ the equation could be written in matrix notation as,

$$\begin{pmatrix} 1 & \omega_c\tau \\ -\omega_c\tau & 1 \end{pmatrix} J = \frac{e^2 n_e \tau}{m} E. \tag{2.14}$$

Using Ohm's law, $\vec{J} = \sigma\vec{E}$ we could obtain an equation for the conductivity σ as,

$$\sigma = \begin{pmatrix} \sigma_{xx} & \sigma_{xy} \\ -\sigma_{xy} & \sigma_{xx} \end{pmatrix} = \frac{\sigma_0}{1+\omega_c\tau}\begin{pmatrix} 1 & -\omega_c\tau \\ \omega_c\tau & 1 \end{pmatrix}. \tag{2.15}$$

Where $\sigma_0 = e^2 n_e \tau/m$, which is the conductivity in the absence of a magnetic field. Now the resistivity, ρ of the system could be written as,

$$\rho = \sigma^{-1} = \begin{pmatrix} \rho_{xx} & \rho_{xy} \\ -\rho_{xy} & \rho_{yy} \end{pmatrix} = \frac{1}{\sigma_0}\begin{pmatrix} 1 & \omega_c\tau \\ -\omega_c\tau & 1 \end{pmatrix}. \tag{2.16}$$

From this equation we get,

$$\rho_{xx} = \frac{\sigma_{xx}}{\sigma_{xx}^2 + \sigma_{xy}^2} \quad , \quad \rho_{xy} = \frac{\sigma_{xy}}{\sigma_{xx}^2 + \sigma_{xy}^2}. \tag{2.17}$$

Applying an electric field in x directions introduces a current density J_x, the charge carrier of this current faces a perpendicular Lorentz force along y direction exerted by the magnetic field applied

along z direction. This results in the building up of an electric field E_y which is responsible for the Hall voltage V_H or V_{xy}. Eventually, at the equilibrium (i.e. $J_y = 0$) we could define another significant parameter, which is the Hall coefficient, R_H which only depends on the carrier density and independent of other material parameters.

$$R_H = \frac{E_y}{BJ_x} = -\frac{1}{n_e e}. \tag{2.18}$$

2.5 Magneto transport in GaAs/AlGaAs heterostructure

As mentioned before, recent development had led to high-quality GaAs/AlGaAs 2D electron systems with motilities in the range of $\times 10^7 cm^2 V^{-1} s^{-1}$. Those samples had led to many new quantum mechanical observations such as Quantum Hall Effect (QHE) [22, 23], Shubnikov de Hass (SdH) oscillations [24], Weak localization (WL) like effects [25], microwave-induced magneto resistant oscillations (MIMOs) [7, 26], etc. Here in this chapter, we will briefly discuss some of those magneto-resistant effects. Figure 3-1 illustrates a schematic of a 2DES with a current I flowing along x direction subjected to a magnetic field $\vec{B}$ along z direction.

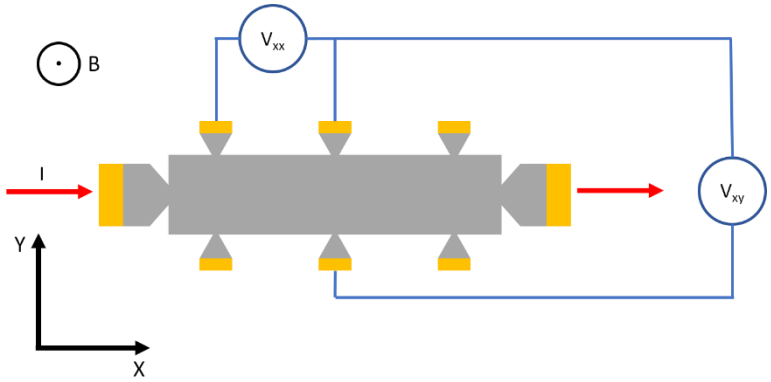

Figure 2.4 Schematic of a Hall Bar structured 2DES used to measure magneto resistant. GaAs/AlGaAs sample is fabricated to have the illustrated structure to measure Hall and diagonal resistance for the experiment. A current is provided from the source terminal, and the current comes out from the drain terminal. The sample sits at a perpendicular magnetic field. Electron motion is allowed only in the XY plane. The longitudinal voltage, V_{xx} and the transverse voltage V_{xy} is used to measure the longitudinal resistant R_{xx} and Hall resistant R_{xy}.

The Longitudinal resistant R_{xx} and the transverse resistant R_{xy} could be calculated by using Ohm's law $R = V/I$. For a constant field and homogenous current flow in the 2DES, we could write the current density along x and y direction as

$$J_x = \frac{I}{W} \quad , \quad J_y = 0 \, . \tag{2.19}$$

Here, W is the width of the Hall bar geometry. If L is the distance between two contacts using Ohm's law, we could write

$$\rho_{xx} = \frac{E_x}{J_x} = \left(\frac{V_x}{L}\right)\left(\frac{W}{I}\right) = \left(\frac{W}{L}\right) R_{xx} \, . \tag{2.20}$$

$$\rho_{xy} = \frac{E_y}{J_x} = \left(\frac{V_y}{W}\right)\left(\frac{W}{I}\right) = R_{xy} \, . \tag{2.21}$$

When we design our Hall bar geometry in such a way that $W = L$, then we end up with

$$\rho_{xx} = R_{xx} \quad , \quad \rho_{xy} = R_{xy} \, . \tag{2.22}$$

2.6 Quantum Hall Effect

Electrons confined two-dimensionally exhibit surprising quantum effects at cryogenic temperatures. Quantum Hall Effect is one of the widespread phenomena where the longitude resistance vanishes and the transverse or hall resistance becomes constant with a value $h/\upsilon e^2$, where υ is an integer, over a specific range of magnetic fields. The high precision of the quantization at the value $R_K = h/e^2 = 25812.807557(18)\,\Omega$ is known as the von Klitzing constant, named after Klaus von Klitzing, who discovered this phenomenon in 1980[1]. The quantization of hall resistance at integer values is known as Integer Quantum Hall Effect (IQHE). This allowed the introduction of a standard resistance independent of the sample and depended only on the Plank constant and the elementary electron charge. The change in the hall resistivity

ρ_{xy}, and the longitudinal resistant ρ_{xx} observed by von Klitzing et. al. in 1986 is shown in figure 2.5[1].

QHE attracted so much attention both theoretically and experimentally. Its microscopic picture could be understood either using the notion of extended and localized states due to disorder[1, 22] or by the edge state picture[27, 28].

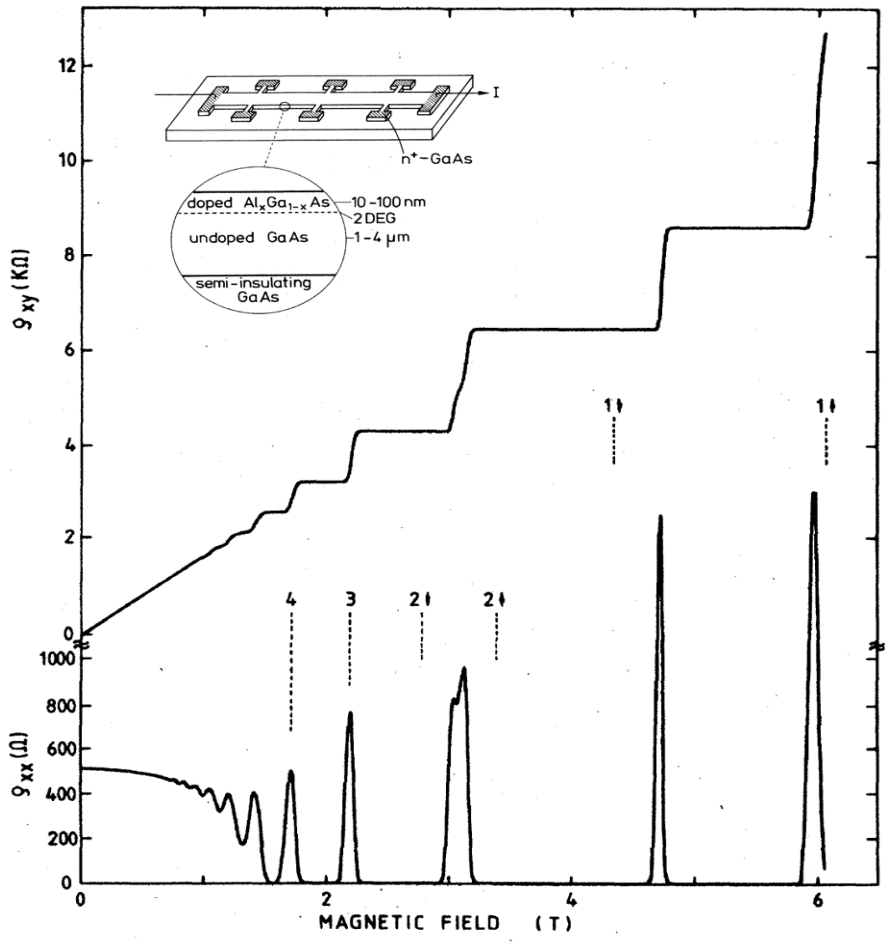

Figure 2.5 The experimental curve for Hall resistance and the longitudinal resistance of a GaAs/AlGaAs heterostructure with the magnetic field at the temperature of about 8 mK [1]. Observation by von Klitzing et al. in 1986 for Hall resistance, $R_H = \rho_{xy}$ and the longitudinal resistance, $R_{xx} \sim \rho_{xx}$ of a GaAs/AlGaAs heterostructure. Hall resistance curve shows plateaus at integer filling factor values while the diagonal resistance exhibits zero resistance states (ZRS). This effect is known as the Integer Quantum Hall Effect (IQHE).

Localized states do not carry current at low-temperature, while the extended states near unperturbed LL could carry electric current. The system's Fermi level could be shifted either by changing the carrier density or varying the magnetic field. Whenever the Fermi level is in a localized region. The occupation of extended states does not change. Thus, we could observe constant Hall resistance or a Hall plateau. Simultaneously, the longitudinal resistance vanishes since no current flow when the Fermi level is at a localized region. When the Fermi level lies in an extended region, the system exhibit dissipation until the Fermi level reaches the next localized state.

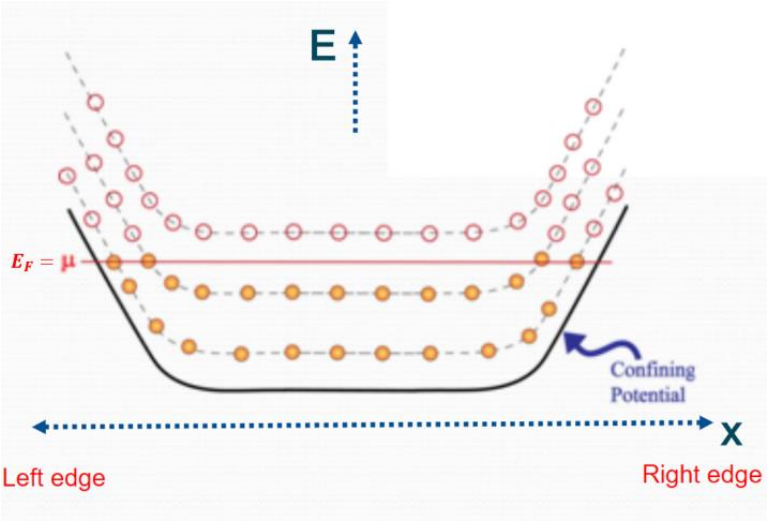

Figure 2.6 Landau Level energy bending due to confining potential with respect to the edge state transport theory for Quantum Hall Effect. The energy diagram of a 2DES with an infinite confining potential at the edge of the sample subjected to a perpendicular magnetic field. Confined potential bends LLS at the edge of the sample creating a one-dimensional ballistic transport channel for electron for a dissipationless transport at particular magnetic fields[6].

In the edge state picture[28], a dissipationless current flow occurs along the sample edge when the magnetic field suppresses the backscattering. The confined potential bends the LL upwards at the sample edge forming one-dimensional ballistic transport channels at the sample's boundary, as shown in figure 2.6.

The advancement of sample fabrication allowed scientists to achieve samples with the reduced disorder. Tsui et al. [29] discovered that in certain devices with a reduced disorder, quantum Hall plateaus could be observed at places where filling factor υ in not a integer but a rational fractional value[29, 30]. This was named as Fractional Quantum Hall Effect (FQHE). Initial observation of FQHE was done at $\upsilon = 1/3$. Since then, many research groups have observed and continue to observe Hall-resistant quantization at many different fractional fillings. FQHE represents new experimental observations resulting in theories leading to the transport of fractionally charged quasi-particles in many-electron systems.

2.7 Shubnikov de Hass Oscillations

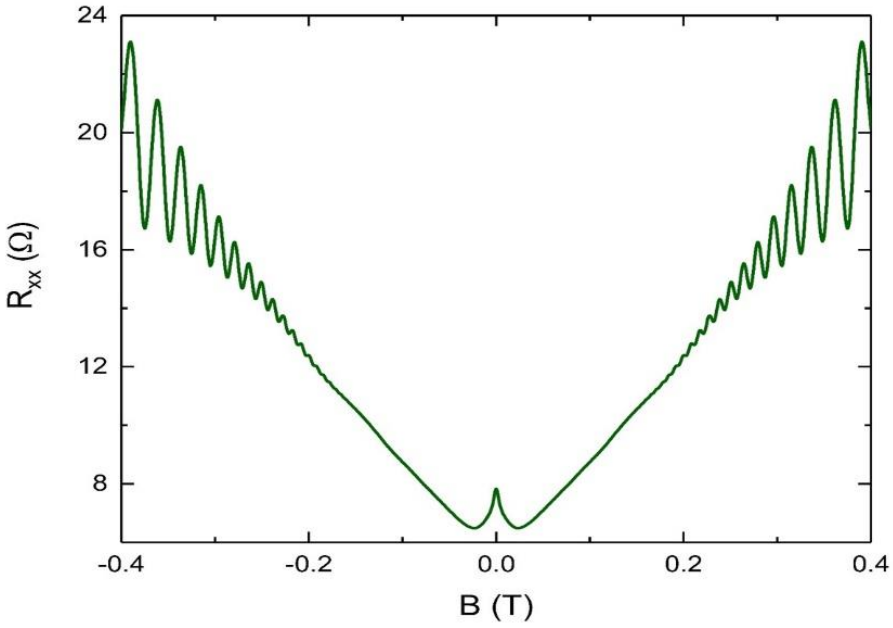

Figure 2.7 Shubnikov de Hass oscillations of a GaAs/AlGaAs heterostructure 2DES at temperature $1.5\ K$*. Lower magnetic fields create overlapping LLs, making the density of states (DOS) periodic and continuous with the inverse magnetic field. The result is the oscillations on diagonal resistance observed, which are known as Shubnikov de Hass (SdH) oscillations (experimental results by Mani and Binuka yet to be published).*

As mentioned in section 2.3, when a 2DES is subjected to a magnetic field, it forms highly degenerate energy levels called LL. In the presence of relatively lower magnetic fields than the fields used to observe QHE, those energy levels are not entirely well separated. The density of states becomes continuous and periodic with inverse B. Such periodicity results in oscillation of longitudinal resistance as a function of magnetic field B as shown in figure 2.7. Those oscillations are known as Shubnikov de Hass (SdH) oscillations.

SdH oscillations are of quantum mechanical origin. The longitudinal resistance during such oscillations never reaches zero, and the Hall resistivity does not show any plateaus. But, SdH oscillations are very helpful in determining material parameters such as the effective mass of carriers m^*, carrier density n, carrier temperature T_e, quantum particle scattering time τ_s, etc.

Background subtracted oscillatory longitudinal resistance in the SdH oscillation region could be fitted by the following equation [31].

$$R_{xx} = R_0 \frac{\chi_T}{\sinh(\chi_T)} e^{-\left(\frac{\pi}{\tau\omega_c}\right)} cos\left(2\pi \frac{E_F - E_N}{\hbar\omega_c} - \phi\right). \tag{2.23}$$

where R_0 is the zero-field resistance, E_N is the energy of Nth state sub-band and χ_T is given by,

$$\chi_T = \frac{2\pi^2 k_B T}{\hbar\omega_c}. \tag{2.24}$$

2.8 Microwave Induced Magneto Resistance Oscillations

Microwave Induced Magneto Resistance Oscillations (MIMOs) is one of the most exciting effects, which was discovered by Mani et al. in 2002 [32] and Zudov et al. in 2001 [26] and was extensively studied both theoretically and experimentally since then. A schematic of the 2DES

setup is shown in figure 2.8. Here the 2DES is at cryogenic temperatures with a current flowing from drain to source.

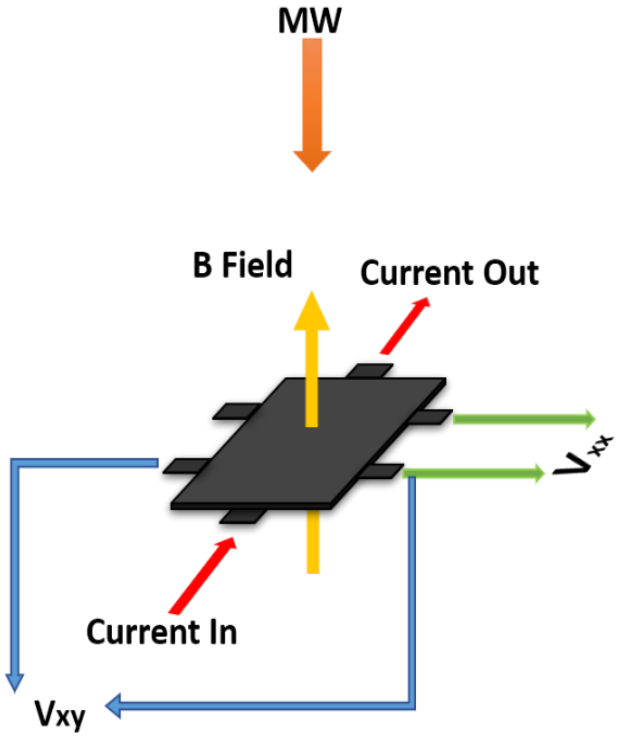

Figure 2.8 A simple setup of the experiment to observe Microwave Induced Magneto Resistance oscillations. GaAs/AlGaAs 2DES is placed in a perpendicular magnetic field. Diagonal voltage, V_{xx} and the Hall voltage, V_{xy} was used to calculate the corresponding resistances. Additionally, the sample was illuminated with Microwave (MW) radiation at the magnetic field ranging from $-0.4\ T$ to $+0.4\ T$.

As shown in figure 2.9, a magnetic field is swept from $-0.4\ T$ to $+0.4\ T$. When Microwave (MW) does not illuminate the sample, we would observe a longitudinal resistance, as shown in the graph by a red curve. When the sample is illuminated by MW radiation, the longitudinal resistance exhibits massive oscillatory behavior, as shown in the graph by a blue curve.

One of the most important phenomena in MIMOs is that it exhibits Zero resistant states (ZRSs) likewise in QHE, but unlike in QHE, we do not observe any Hall Plateaus in the Hall resistance R_{xy}. The behavior of MIMOs has yet to be understood with many experimental [9, 10,

26, 32-42] and theoretical research [3, 4, 8, 43-49] addresses this problem. As shown in figure 2.9, ZRS could be observed at the points where,

$$B = \left(\frac{4}{4+j}\right) B_f \, . \tag{2.25}$$

Here, $j = 1,2,3,$ ... and $B_f = 2\pi f m^*/e$ where f is the MW radiation frequency. MIMOs are also periodic with the inverse magnetic field. Also, they could be fitted to exponentially damping sinusoidal function [10] as

$$\Delta R_{xx} = -A_0 e^{-\left(\frac{\lambda}{B}\right)} \sin\left(\frac{2\pi B_f}{B}\right). \tag{2.26}$$

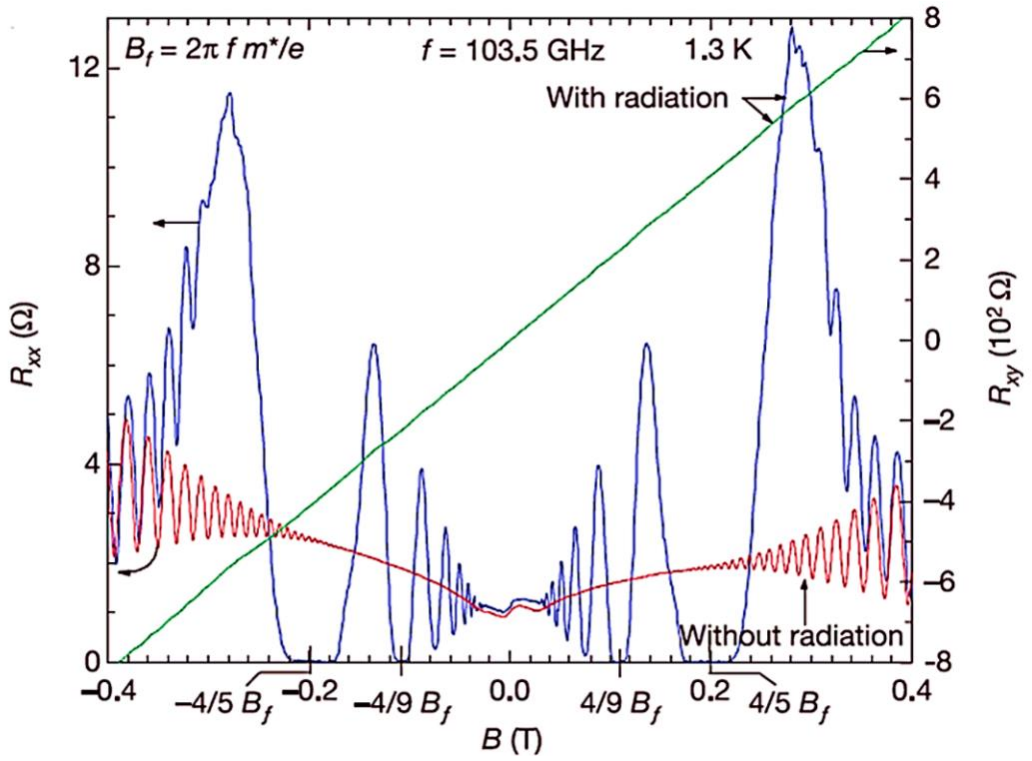

Figure 2.9 The behavior of diagonal (R_{xx}) (left y-axis) and Hall (R_{xy}) (right y-axis) resistance of GaAs/AlGaAs 2DES subjected to MW radiation with perpendicular magnetic field exhibiting the Zero Resistance States[7]. With no MW radiation, the diagonal resistance of the sample lineshape (red line) exhibits SdHs oscillations. 103.5 GHz MW irradiation induces an oscillatory diagonal resistance behavior (blue line) with ZRSs at $B = (4/4 + j)B_f$ magnetic fields, while the Hall resistance (green line) does not exhibit any plateaued effect as in IQHE. The diagonal and the Hall resistance values are at left and right y-axises, respectively.

Here, A_0 is the MIMO amplitude, λ damping factor and B_f is the MIMO oscillation frequency with respect to the inverse magnetic field B. There are different theoretical models to explain MIMOs, such as Displacement Model[8], Non-Parabolicity Model[4], the Inelastic Model[48], Radiation Driven Electron Orbit Model[3], etc.

2.8.1 Displacement Model

One way of explaining the MIMO behavior is to use the effect of radiation-induced disorder-assisted current, also known as the Displacement Model suggested by A. C. Drust et al. (2003). In the presence of disorder, LLs are broadened. When the sample is illuminated by MW radiation, the electrons absorb photons' energy and are excited to higher Landau energy levels.

In the absence of disorder, the conductivity of the 2DES does not depend on the electron distribution in LL, as suggested by Kohn's theorem[50]. In this scenario, photo-excited electrons do not change the amount of current flow through the 2DES. In the presence of disorder, electrons could be scattered by impurities as they are photo-excited. A highly simplified picture of the the process is shown in figure 2.10 [8].

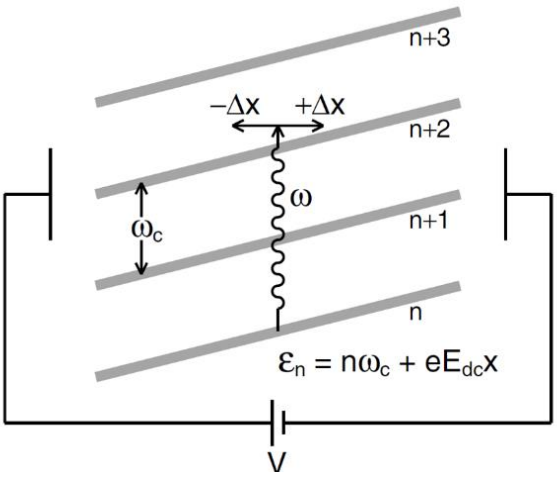

Figure 2.10 A Simplified picture of radiation-induced disorder assisted model suggested by A. C. Drust et al.[8]. The applied magnetic field forms LLs, and they are tilted due to the applied electric field across the sample. Incoming MW photon excites the electron to a higher LL. Disorders in the sample scatter the excited electron to left or right depending on the distance $-\Delta x$ and $+\Delta x$ to an allowed energy level which increases or decreases the resistance, respectively.

The applied bias voltage tilts the LLs as shown in figure 2.10, the photoexcited electrons get scattered to the left or the right by a distance of $\pm\Delta x$ by impurities, see figure 2.10. If the final density of the states to the left is higher than the one to the right, electric current is enhanced by the scattering and vice versa. As the magnetic field changes, the separation between LL changes with B, thus resulting in an oscillatory behavior in the longitudinal resistanceR_{xx}.

2.8.2 Non-Parabolicity Model

The dc conductivity, σ_{dc}, changes only when the Kohn theorem[50] is violated. Commonly assumed Kohn violation is due to impurities, here instead of the impurities A. A. Koulakov et al. (2003)[4] have considered a weak non-parabolicity of electron spectrum, which could also violate the Kohn theorem resulting in changing in σ_{dc}. The linearly polarized MW radiation introduces an ac electric field. In this model, it was shown that the ac linearly polarized electric field could change the σ_{dc} in the presence of a weak non-parabolicity of electron spectrum.

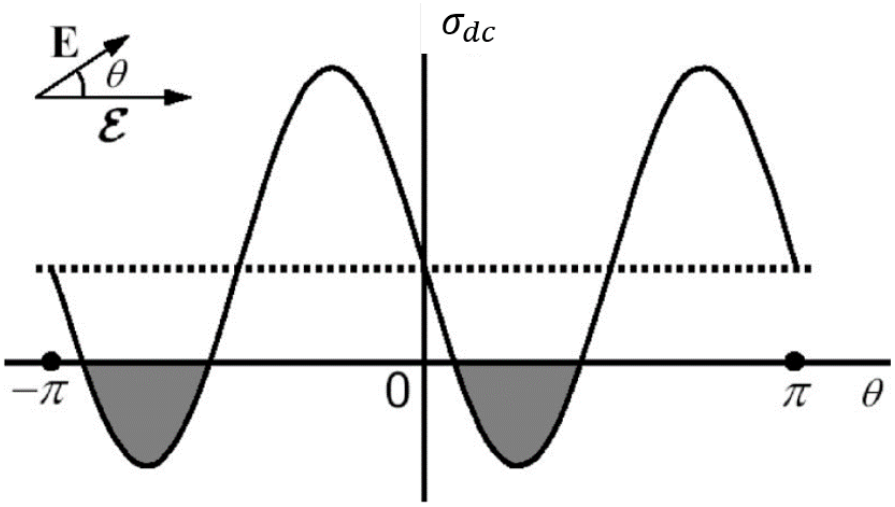

Figure 2.11 The diagonal conductivity (σ_{dc}) as a function of the angle θ between ac, ε and dc E electric fields illustrated in the inset[4]. The dashed line shows the conductivity under no MWs. The solid curve is a plot of the diagonal conductivity under irradiation obtained by the non-parabolicity model. It assumes negative values within the angular intervals shown with gray.

In figure 2.11, the dashed line indicates the dark conductivity. The solid sinusoidal plot is the σ_{dc}. Inset shows the angle between the dc, E and ac electric fields, ε. Conductivity, σ_{dc}, becomes a negative in the shaded region.

As the radiation power increases the σ_{dc} becomes zero for a particular value of θ. Further increase of radiation power widens the negative σ_{dc} region. But this model could only explain the behavior of σ_{dc} near the cyclotron resonance but not at the harmonics of the cyclotron resonance, where the oscillatory behavior of the longitudinal resistance is also observed. Additionally, the model could only explain the MIMO assuming a linear polarization of the MW radiation. Still, experimentally it was proven that the MIMOs could also be observed even under circularly polarized MW radiation[51].

2.8.3 Inelastic Model

I. A. Dmitriev et al. have described the effect of MIMOs as a result of the change of an electron distribution function induced by MW radiation[45]. This model suggests that the MIMO and the ZRS can be understood as a result of the oscillatory photoconductivity. The oscillatory photoconductivity is governed by the radiation-induced change in the electron distribution function. Oscillations in Density of State (DOS) are related to LL quantization, leading to an oscillatory correction to the distribution function.

This model suggests that the dc conductivity varies with ω/ω_c and is proportional to the inelastic relaxation time of 2DES. The model could explain the behavior of MIMOs with the temperature, MW power using the dependency of the inelastic relaxation time on those physical variables. However, this model fails to explain the experimentally observed polarization dependency of the MIMO.

2.8.4 Radiation Driven Electron Orbit Model

J. Iñarrea et al. describe the MIMOs using an exact solution of the harmonic oscillator wave function in the presence of radiation and applying perturbation treatment for elastic scattering caused by randomly distributed charged impurities [52]. This model could be used to explain the resistive oscillation formation, their frequency, power dependency, temperature effect on them, and resistive minima locations as a function of the magnetic field.

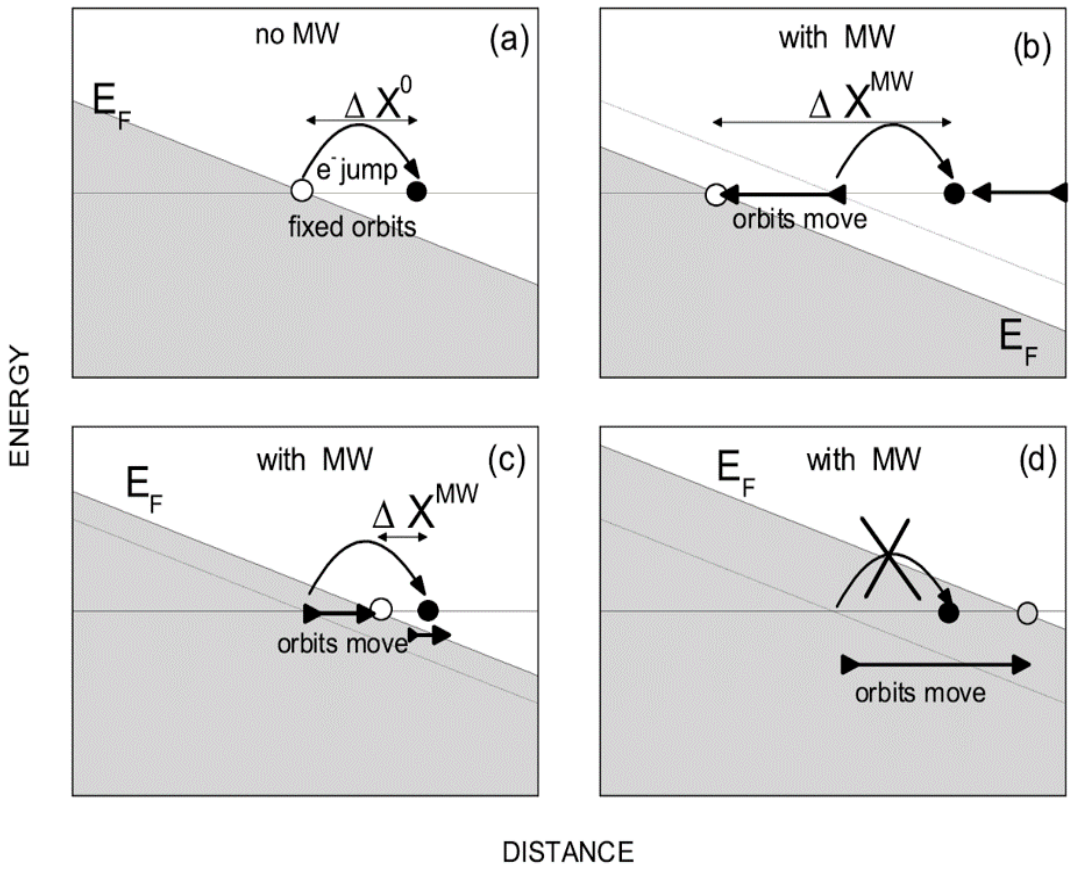

Figure 2.12 Schematic diagram of electron transport in GaAs/AlGaAs 2DES according to the radiation driven electron orbit model[3]. (a) Electron jump between fixed electron orbits without any MW irradiation, (b) electron jump between orbits while the orbit moves backward, increasing the total electron advancement increasing the conductivity, (c) electron jump between orbits while the orbit moves forward, decreasing the total advancement thus decreasing the conductivity, (d) electron jump is restricted because the orbit moves further than the electron advancement.

As illustrated in figure 2.12, electrons absorb energy from photons and jump between orbits. When the sample is not illuminated with MW radiation, the electron orbits are fixed. In this case, electrons jump an average distance ΔX^0. The MWs result in oscillations of the electron orbits back and forth. If, as shown in figure 2.12 (b), electron orbit moves backward while the electron jumps, the electron advances a larger distance $\Delta X^{MW} > \Delta X^0$ compared to the case when there is no radiation. This results in an increase in conductivity. If electrons jump while the orbit moves forward, then as shown in figure 2.12(c) $\Delta X^{MW} < \Delta X^0$. If the MW power is high enough, the orbits could oscillate a higher distance than the one the electron could jump. This restricts the electron advancement due to the Pauli exclusion principle, which could be identified as ZRS in longitudinal resistance.

3 EXPERIMENT ON BICHROMATIC MICROWAVE INDUCED MAGNETORESISTANCE OSCILLATIONS

GaAs/AlGaAS 2DES hall bar configuration is used for this experiment. Hall bar sample was cooled down to base temperatures of about 1.7 K. The sample was illuminated by two microwave radiation sources with different frequencies, and bichromatic Microwave Induced Microwave Oscillations (bMIMO) were observed in the diagonal resistance R_{xx}. Different aspects of those bMIMOs were examined experimentally, and a qualitative explanation was developed to explain the experimental data for dual microwave excitations.

3.1 Setup to observe MIMOs

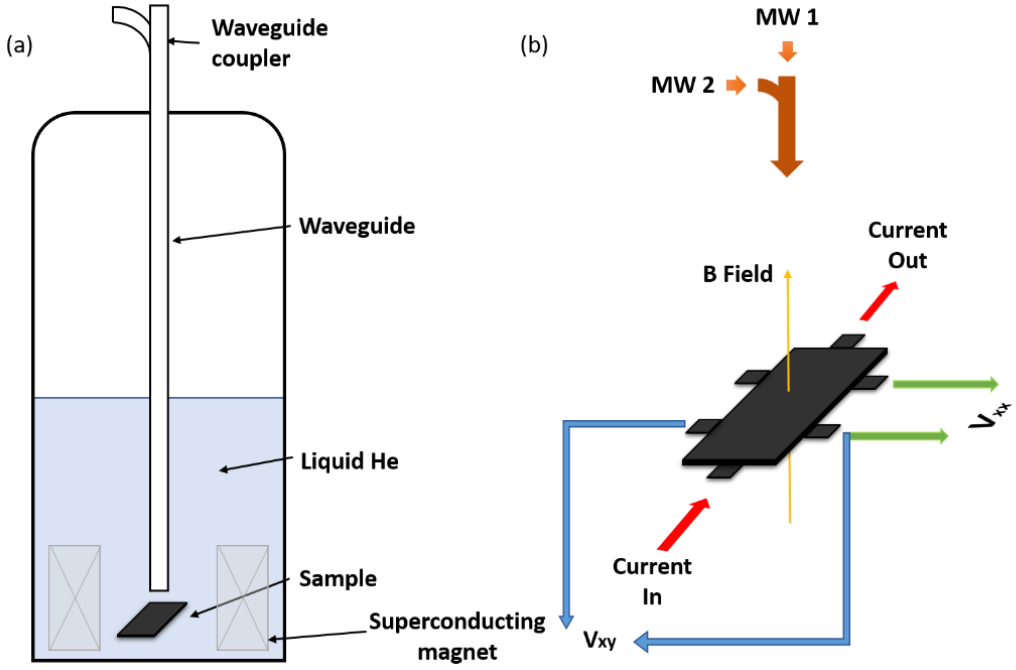

Figure 3.1 Sample setup (a) The sample placed inside a cryostat filled with LHe4 (b) Simple sample configuration to observe bMIMOs. GaAs/AlGaAs sample is placed in a cryostat filled with LHe4. A vacuum pump is used to pump on the LHe4; the process cools down the sample to 1.7 *K. A superconducting magnet provides a perpendicular magnetic field for the 2DES. A waveguide is used to transport the MW radiation. A waveguide coupler at the top is used to irradiate the sample with two MW radiations simultaneously.*

As shown in figure 3.1(a) sample is placed inside Liquid He-4 (LHe4). Using LHe4, we could lower the sample temperature to $\sim 4.1\ K$. But for this experiment, we have pumped on liquid He to go to even lower temperatures closer to $1.7\ K$. A magnified version of a simplified sample configuration is shown in figure 3.1(b).

Initially, the measurement was carried out on a GaAs/AlGaAs 2DES with an electron density of $3.3 \times 10^{11}\ cm^{-2}$ and mobility of $1.5 \times 10^{6}\ cm^{2}/Vs$. Two microwave sources at different frequencies were coupled using a waveguide coupler to produce photoexcitation. A long cylindrical waveguide carries the produced microwave to the sample in a liquid Helium bath. It should be noted that the two microwaves that are used are both polarized in the same direction. The single monochromatic high frequency, f_1, initially illuminated the sample, with the low frequency, f_2, microwave source switched off, and vice versa to illuminate the sample from low frequency f_2. Both f_1 and f_2 MW sources were turned on simultaneously to achieve dual-frequency photoexcitation.

3.2 bMIMO dependency with the magnetic field

Initially, the line shape of the bMIMO was compared with monochromatic MIMOs of the two frequencies used to produce the bi-chromatic MW. It is important to indicate that we have considered the resistance change due to electron heating[33, 40, 42] from MWs to be negligible. To elaborate more, we assumed that since we have used low enough MW powers, the electron heating effect is the same for two monochromatic frequencies f_1 and f_2, and also it is the same for bichromatic frequency produced by $f_1 + f_2$ for the magnetic field region we sweept. Here, the magnetic field sweep rate used for the experiment is minimal to have a stable temperature throughout. It was observed experimentally that the slow enough sweep rates do not affect sample temperature significantly. Figures 3.2 and 3.3 show two monochromatic responses and the

bichromatic response of MIMOs from the $0 - 0.4\,T$ magnetic field region for two different microwave combinations of f_1 and f_2.

In figure 3.2, when the specimen is photoexcited from 90.6 GHz and 41.0 GHz MW radiation, it is observable that two peak points that correspond to 90.6 GHz monochromatic MIMO lineshape coincide with a peak and valley points of 41.0 GHz monochromatic MIMO lineshape at 0.055T and 0.075T, respectively. Similarly, when the specimen is photoexcited from 90.6 GHz and 48.7 GHz MW, two valley points that correspond to 90.6 GHz monochromatic MIMO lineshape coincide with a peak and a valley points of 48.7GHz monochromatic MIMO lineshape at 0.062T and 0.09T, respectively, see figure 3.3. It is also beneficial to observe the evolution of bMIMO lineshape.

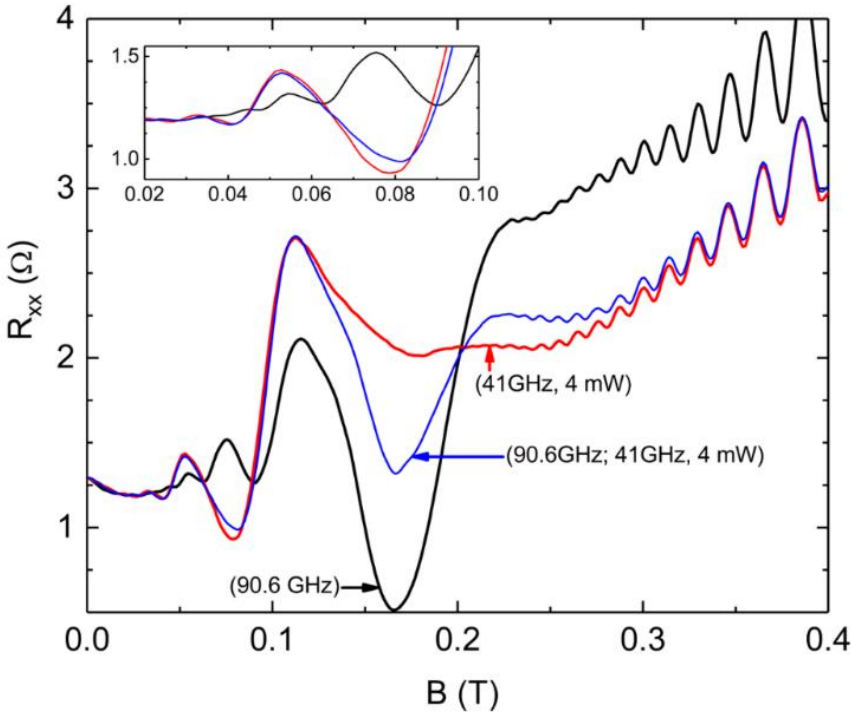

Figure 3.2 Experimental Monochromatic and bichromatic MIMO line shapes of the diagonal resistance for MW frequencies of 41.0 GHz, 90.6 GHz and the combination of the two frequencies. Red: Monochromatic MIMO line shape for 41.0 GHz, Black: Monochromatic MIMO line shape for 96.0 GHz, Blue: bMIMO line shape for the combination of two frequencies for magnetic field regions of 0 T – 0.4 T. Inset: the magnified version of the diagonal resistance line shapes from 0.02 T – 0.1 T. (experimental results by Mani and Binuka obtained from [9]).

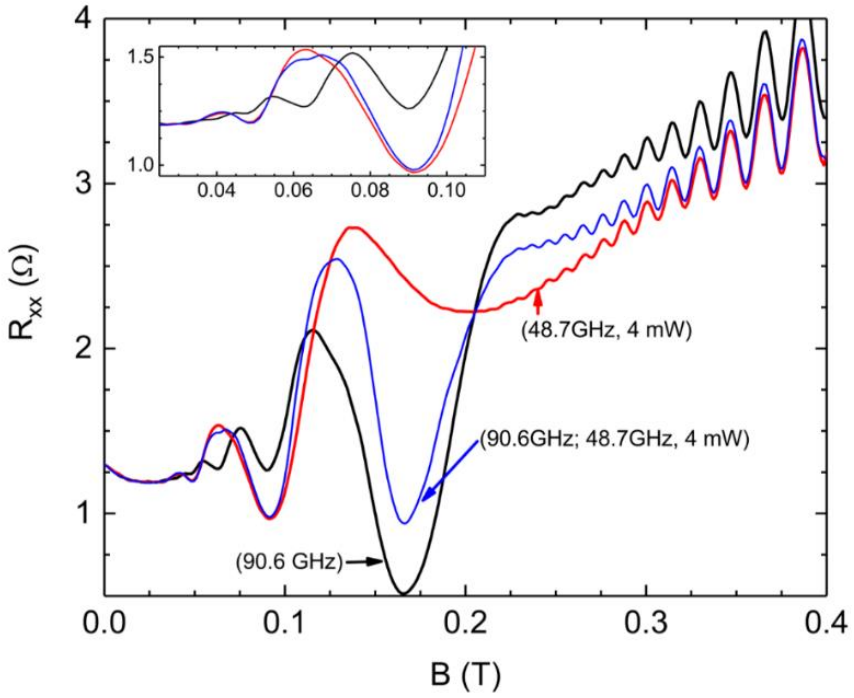

Figure 3.3 Experimental Monochromatic and bichromatic MIMO line shapes of the diagonal resistance for MW frequencies of 48.7 GHz, 90.6 GHz and the combination of the two frequencies. Red: Monochromatic MIMO line shape for 48.7 GHz, Black: Monochromatic MIMO line shape for 96.0 GHz, Blue: bMIMO line shape for the combination of two frequencies for magnetic field regions of 0 T – 0.4 T. Inset: the magnified version of the diagonal resistance line shapes from 0.02 T – 0.12 T (experimental results by Mani and Binuka obtained from [9]).

In fact, those specific frequencies were chosen to observe the behavior of such lineshape under the influence of MW power, which will be later described in this chapter. Here to analyze the lineshapes, we could divide our plot in figure 3.2 into three sections, as shown in figure 3.4.

The line shape of the bMIMO in region 1 (blue line) of figure 3.4 follows the low-frequency monochromatic MIMO response (red line) of 41.0 GHz. In region 2, the bMIMO line shape starts to deviate towards the high-frequency MIMO response (black line) of 90.6 GHz. When we increase the magnetic field and arrive at region 3, the bMIMO response mainly exhibits the high-frequency MIMO characteristics. A similar pattern can be identified in the frequency combination of 90.6 GHz and 48.7 GHz shown in figure 3.5, which is regionally divided in figure 3.3.

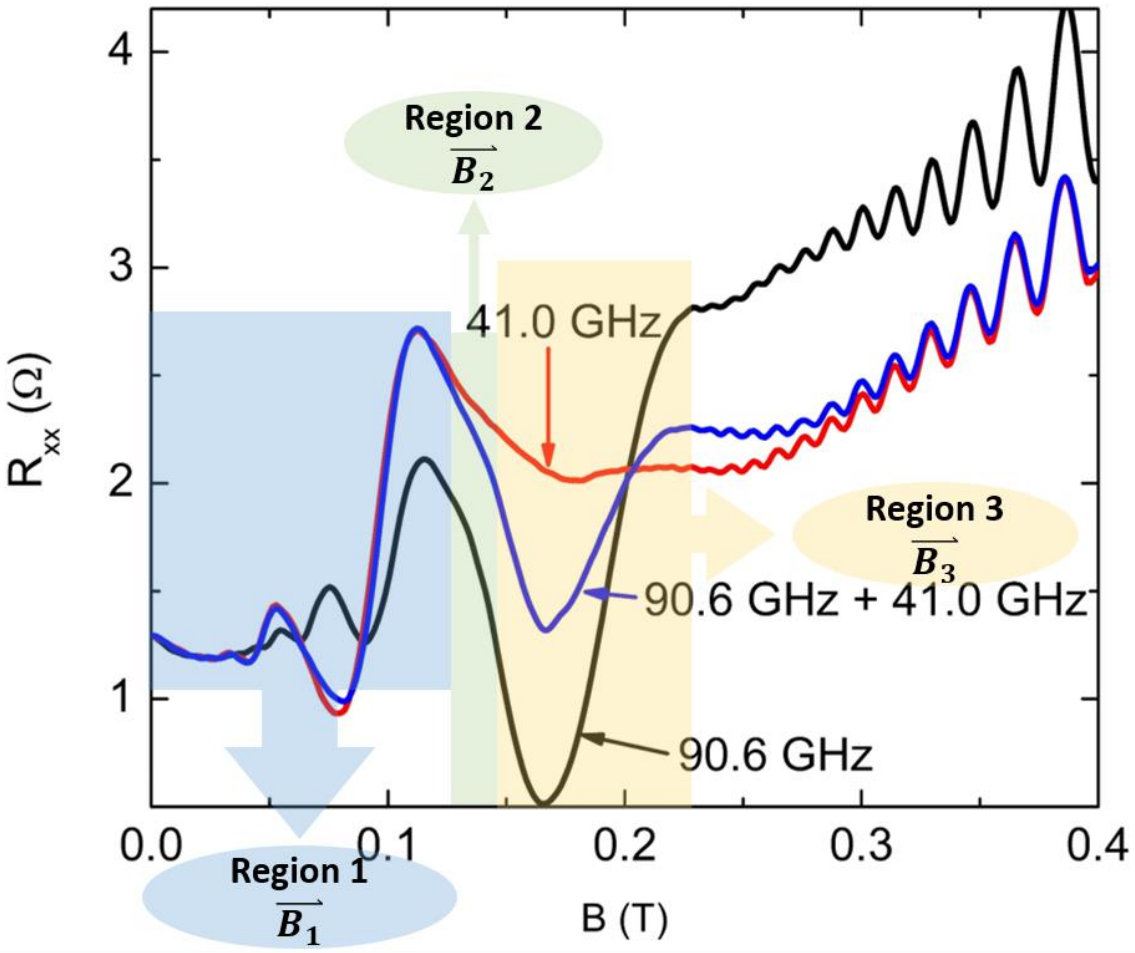

Figure 3.4 Region wisely divided experimental monochromatic and bichromatic MIMO line shapes of the diagonal resistance for MW frequencies of 41.0 GHz, 90.6 GHz. The magnetic field regions are divided as, Region 1: $0 \leq B \leq 0.125\,T$ *(highlighted in light blue), Region 2:* $0.125\,T \leq B \leq 0.15\,T$ *(highlighted in light green), Region 3:* $0.15\,T \leq B \leq 0.225\,T$ *(highlighted in light yellow) to understand the lineshape evolution of the bMIMO behavior (experimental results by Mani and Binuka obtained from [9]).*

The line shape of the bMIMO in region 1 (blue line) of figure 3.5 follows the low-frequency monochromatic MIMO response (red line) of 48.7 GHz. In region 2, the bMIMO line shape starts to deviate towards the high-frequency MIMO response (black line) of 90.6 GHz. When we increase the magnetic field and arrive at region 3, the bMIMO response mostly exhibits the high-frequency MIMO characteristics.

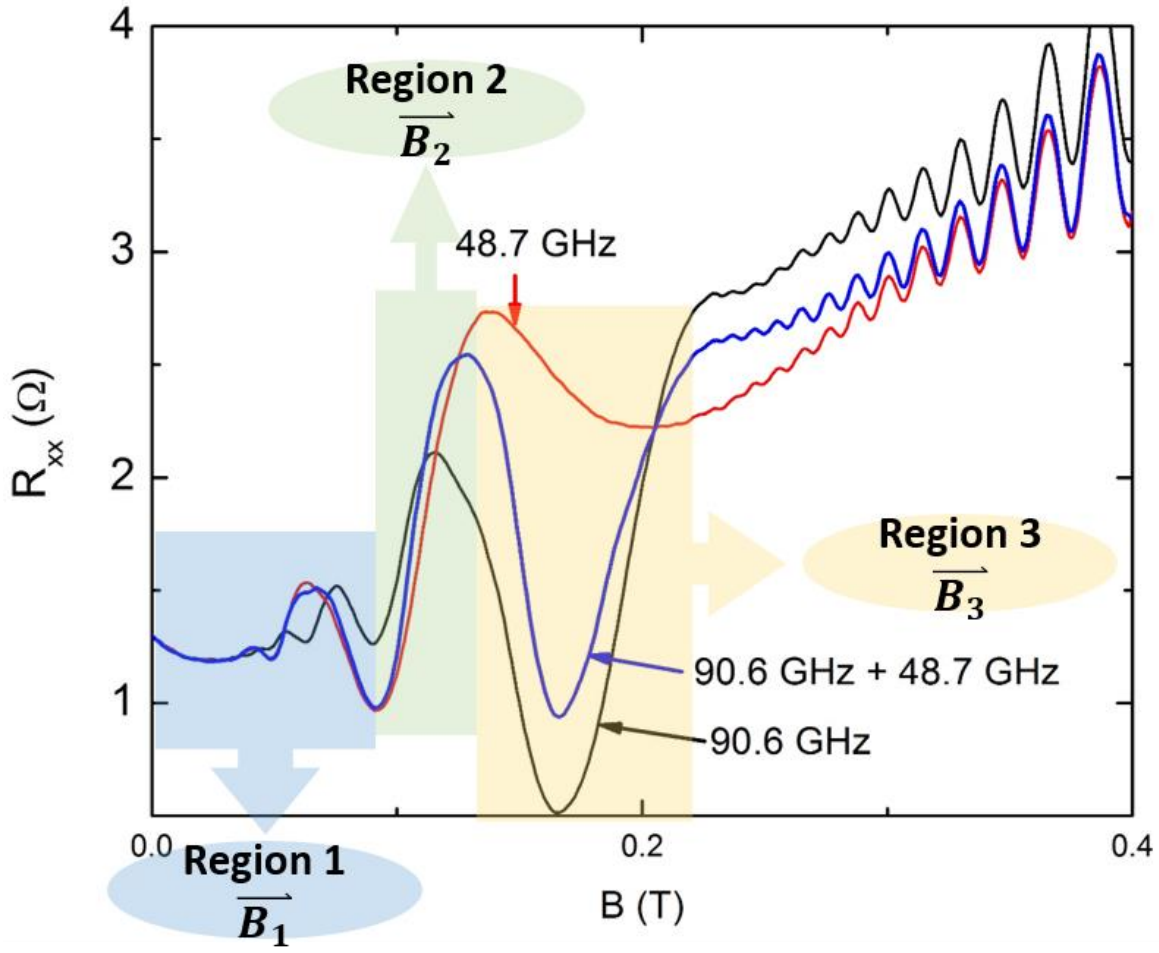

Figure 3.5 Region wisely divided experimental monochromatic and bichromatic MIMO line shapes of the diagonal resistance for MW frequencies of 48.7 GHz, 90.6 GHz. The regions are divided as, Region 1: $0 \leq B \leq 0.095\,T$ *(highlighted in light blue), Region 2:* $0.095\,T \leq B \leq 0.125\,T$ *(highlighted in light green), Region 3:* $0.125\,T \leq B \leq 0.215\,T$ *(highlighted in light yellow) to understand the lineshape evolution of the bMIMO behavior (experimental results by Mani and Binuka obtained from [9]).*

This result is somewhat different from the experimental results previously obtained by different groups[5]. In their observation, they have considered different frequency combinations than the ones we used, which are $f_1 = 47.0\,GHz$ and $f_2 = 31.0\,GHz$ with ratio between frequencies $f_1/f_2 \approx 1.5$. In their observation they have found out that the both frequencies contribute to the bichromatic lineshape independent of the magnetic field. Their observation is shown in figure 3.6.

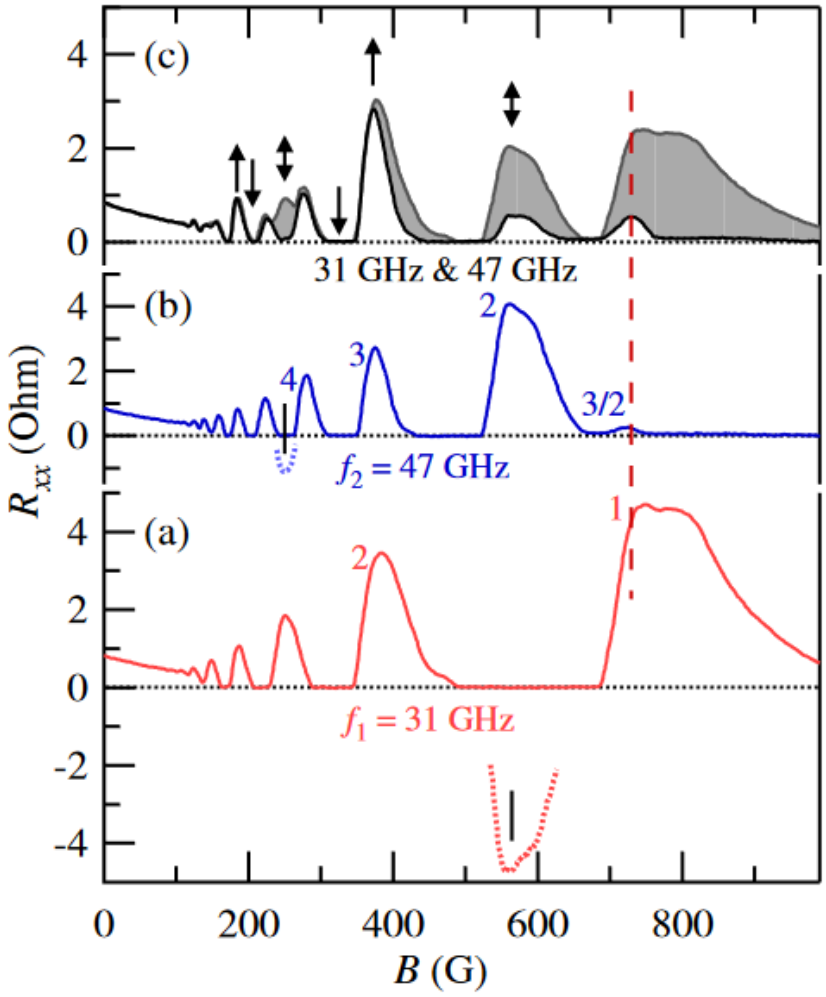

Figure 3.6 bMIMO behavior observed by Zudov et al. in 2006[5] under monochromatic and bichromatic MWs with MW combination of 47 GHz and 31 GHz. Panels (a) and (b) show magnetoresistance data for monochromatic MW of 31 GHz and 47 GHz, respectively. Numbers on top of curves are harmonics of cyclotron resonance. Panel (c) solid line represents the bMIMO behavior, and the shaded area represents the average of two monochromatic responses, 31 GHz and 47 GHz. Peak-peak, valley-valley, peak-valley overlaps are marked by ↑, ↓ and ↕ respectively. The dotted line represents the reconstructed negative resistance from equation 3.1.

Our result shows that the bMIMO response depends on the magnetic field and frequency. Ratios of the frequencies we have used are $f_1/f_2 = 90.6GHz/41.0GHz \approx 2.2$ and $f_1/f_2 = 90.6GHz/48.7GHz \approx 1.9$. To further confirm the magnetic field dependence of the

bMIMO behavior, we have combined several frequencies with higher f_1/f_2 ratios. The results are shown in figure 3.7.

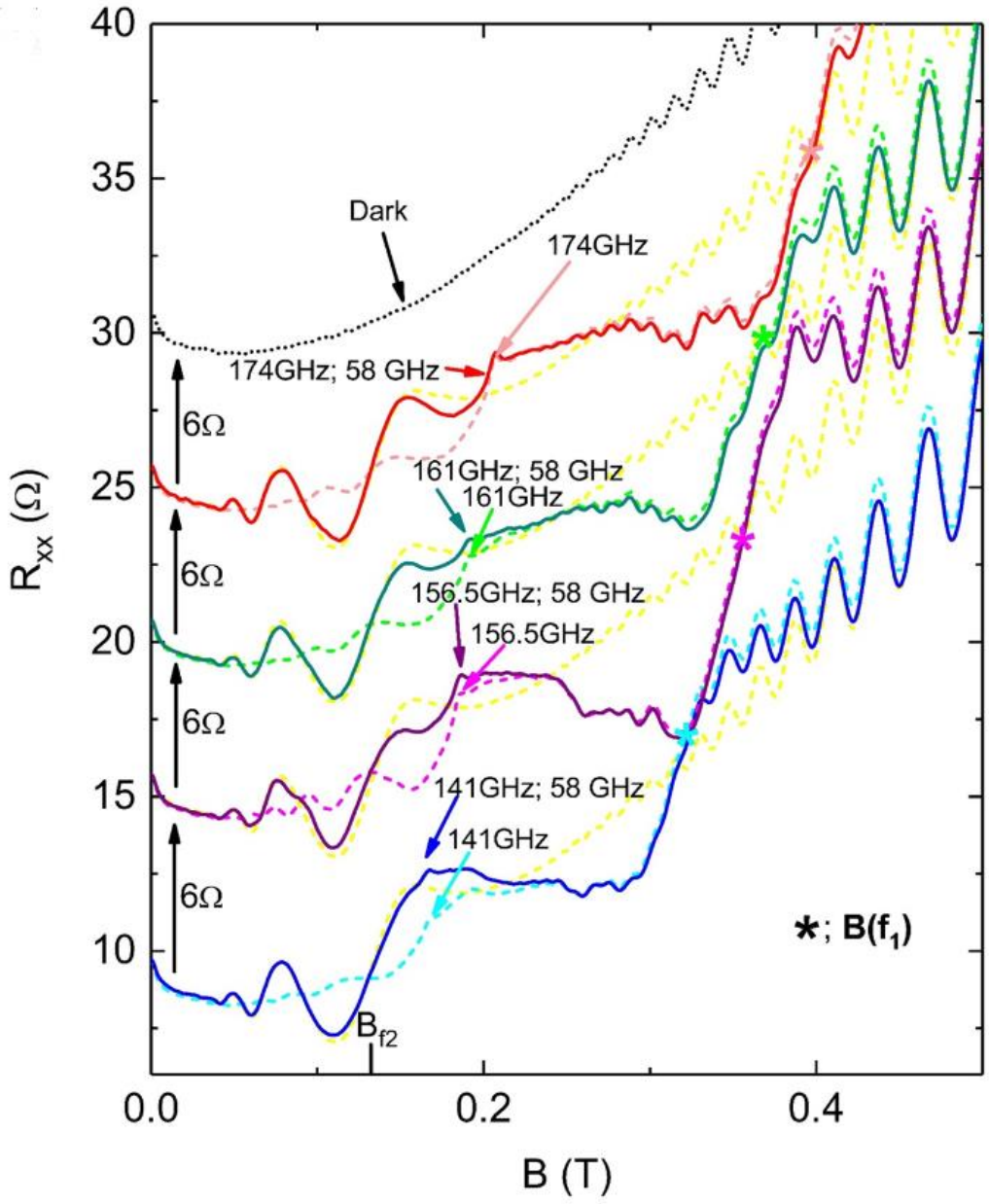

*Figure 3.7 Experimental bMIMO behavior with fixed low frequency f_2 at 58.0 GHz with high frequencies f_1 takes on values 141.0, 156.5, 161.0 and 174.0 GHz[9]. (Color online) Each curve is shifted 6Ω along the vertical axis for clarity. The dotted line exhibit the R_{xx} resistance behavior under no MW illumination. The nominal power for f_1 ranges from 10-20 mW while the source power for f_2 was fixed at 10 mW. The * sign indicated the $\sim 2\omega_c$ of high frequency, and the arrowheads used to point out high frequency showing a small $\sim\omega_c$ points for each f_1.*

Here we have chosen the very high frequencies 141.0, 156.5, 161.0, and 174.0 GHz as f_1 because it could exhibit bMIMO dependency with the magnetic field in a more pronounced manner. We observe that the low-frequency component of the bMIMO dominates the low magnetic field region while the high-frequency component of bMIMO dominates the high magnetic field regions. Here, in figure 3.7, we could not use the same source power at high frequency due to the apparatus's limitations. A study on the power dependency of bMIMO would provide more insight into the matter.

In the previous study done by Zudov et al. [5] on the bMIMO response of GaAs/AlGaAs 2DES system, the line shape behavior has been explained by the following equation, as an average of two monochromatic responses when using the same power for the MW radiations,

$$R_{exp}^{\omega_1\omega_2} = max\{\alpha R^{\omega_1} + (1-\alpha)R^{\omega_2}, 0\}. \quad (3.1)$$

Here $R_{exp}^{\omega_1\omega_2}$ is the bichromatic diagonal resistance, R^{ω_1} is the monochromatic diagonal resistance from MW radiation of 31.0 GHz and R^{ω_2} is the monochromatic diagonal resistance from MW radiation of 47.0 GHz, and

$$\alpha = (1+p)^{-1}, p = \frac{P_2}{P_1}. \quad (3.2)$$

Here P_1 and P_2 are the MW intensities corresponding to MW radiation with a frequency of 31.0 GHz and 47.0 GHz, respectively. Whenever the MW powers are similar, then $\alpha = 0.5$, which suggests that the bichromatic diagonal resistance should be the average of two monochromatic responses. In our experiment, we have also used the same power for both MW sources. Figure 3.8 shows a comparison between the average of two monochromatic responses of 90.6 GHz and 48.7 GHz with the combination's bMIMO response. It is evident that the bMIMO lineshape has the same shape as the average, but it is not overlapping with the average. Thus we could conclude that the bMIMO response depends both on the MW power and the magnetic field.

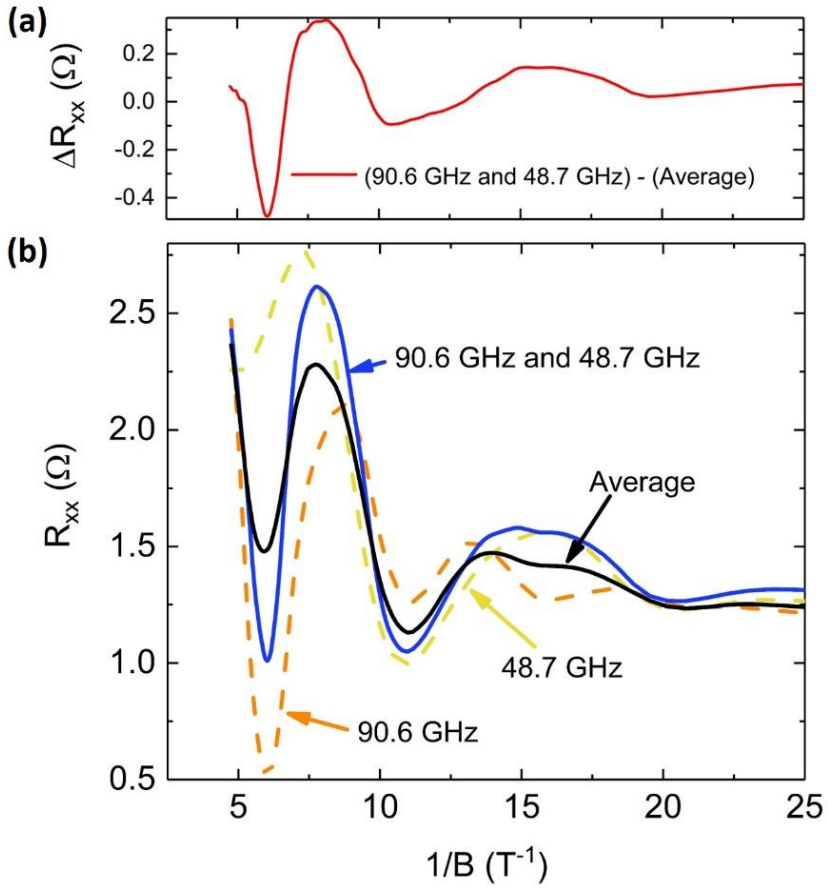

Figure 3.8 Comparison of the arithmetic average of experimental monochromatic MIMO responses 90.6 GHz and 48.7 GHz with the experimental bMIMO response of the frequency combination[9]. (a) the difference between the experimental bMIMO response (blue line in panel (b)) and average of monochromatic MIMO responses (black line in panel (b)). (b) Experimental diagonal resistance, R_{xx} with respect to the inverse magnetic field, $1/B$ for monochromatic responses 90.6 GHz (Orange dashed line), 48.7 GHz (yellow dashed line), the average of two monochromatic responses (black line), and experimental bMIMO response for the frequency combination (blue line).

The magnetic field dependency of bMIMO observed using GaAs/AlGaAS heterostructure samples is a novel phenomenon. So we have developed a model to explain this behavior the diagonal resistance of the samples under dual MW irradiated samples qualitatively as follows.

GaAs/AlGaAs 2DES subjected to a perpendicular magnetic field produces LLs with energy spacing of $\Delta E = \hbar\omega_c$. The DC electric field applied across the sample to drive the current causes LLs to tilt, as shown in figure 3.9.

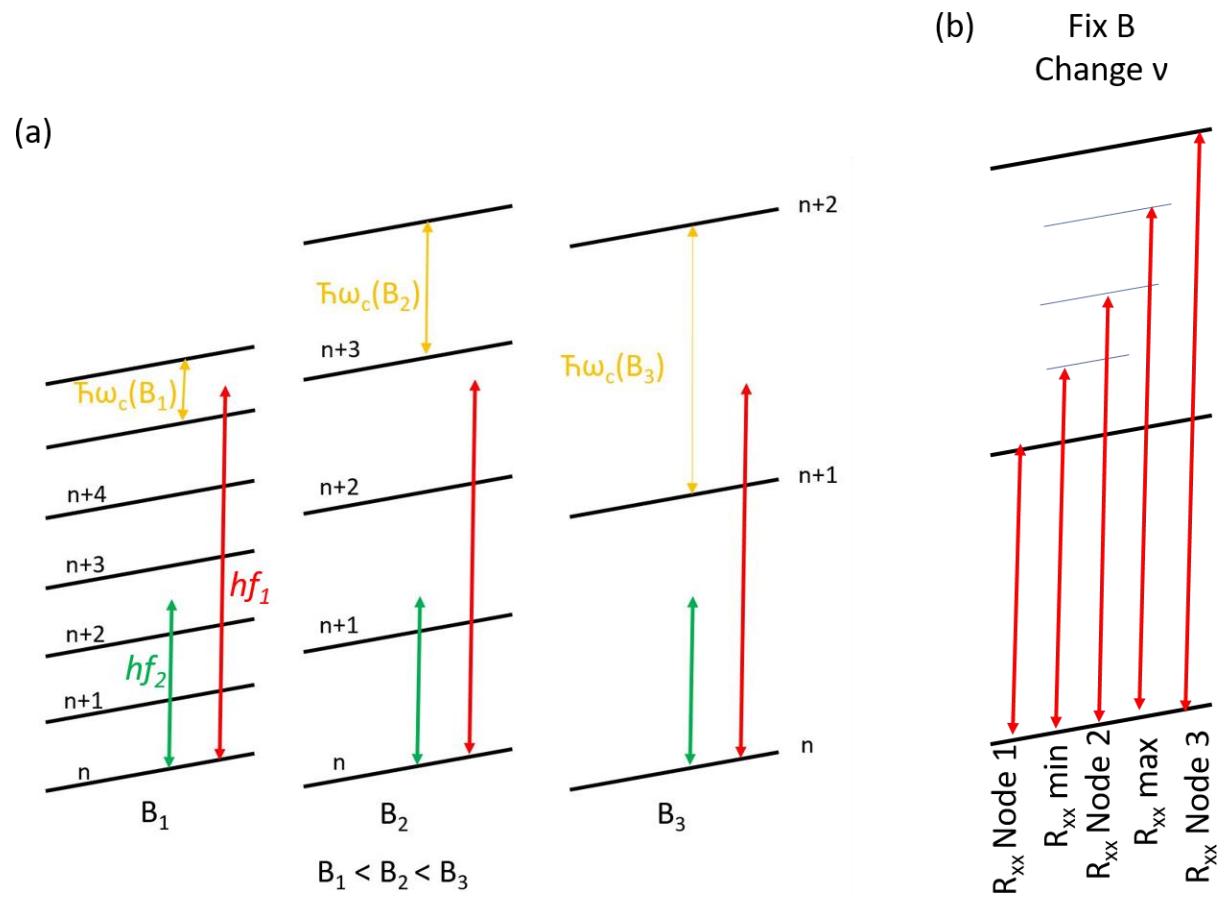

Figure 3.9 Illustration of photon transition due to MW excitation in between LLs in GaAS/AlGaAS 2DES while the sample is carrying a current[9]. (a) with condition $B_1 < B_2 < B_3$ which increases the LL separation satisfying $\Delta E = \hbar\omega_c(B)$. (b) Excitation of an electron from photons with different energies (represented in red arrows) at a constant magnetic field. 2DES is subjected to a perpendicular magnetic field. The red and green arrow illustrates inter LL transition of a photoexcited electron from high and low-frequency MW photons, respectively. The figure conveys that the reason to observe an oscillatory behavior in diagonal resistance R_{xx} is caused because of the order of excitation (number of LLs crossed by the electron while photoexciting from different MW photons). The change of the order of excitation with the magnetic field affects the dominant MW frequency responsible for the majority of electron photoexcitation.

Here, see figure 3.9(b), the electrons could be excited by different photon energies as mentioned earlier in the displacement model[8]. When the photon energy corresponding to the case of R_{xx} Node 1, see figure 3.9(b), we observe a node point in the diagonal resistance. When we increase the photon energy to a situation shown by R_{xx} min point we observe a valley in the diagonal resistance because the impurity scattering enhance the conductivity. Next for R_{xx} Node

2 case, the scattering-effect cancels out. For the case of R_{xx} max point, scattering processes weaken the conductivity and enhance the diagonal resistance. Here the phenomena of the oscillatory diagonal resistance is discussed with a constant magnetic field. In fact, the same procedure applies when we sweep the magnetic field by keeping the photon energy a constant.

The situation in the bichromatic MW excitation is illustrated in figure 3.9(a). Here the photon energies are different. Thus the low and high-frequency photon energies are illustrated by green and red arrows separately. To explain the observed magnetic field dependency of the bMIMOs, we assume that photoexcitation that spans over fewer landau levels gives a larger contribution to the magnetoresistance than the one that spans over a larger number of LLs. This is because that photoexcitation transition probability associated with fewer LL crossing is large. Then, the transition time for an electron to be excited between fewer LLs is shorter. When the electron crosses a higher number of LLs during the photoexcitation process, the transition probability is small, and the transition time is longer. In figure 3.9(a), when the magnetic field is smaller, the number of LLs electrons has to cross, or 'the order of excitation' is two for low and five for high frequency. Thus with the reasoning, the transition that corresponds to the excitation over fewer LLs is dominating. Such transitions correspond to a lower frequency excitation. As we have observed in figures 3.4,3.5, and 3.7, the bMIMO response almost exactly follows the low-frequency monochromatic response behavior at a lower magnetic field region.

Next, we increase the magnetic field and arrive at the magnetic field region B_2. The order of excitation from low and high-frequency MWs are in the range of one and three. Here also, the low-frequency response of the bMIMO should dominate. But, since the order of excitation of higher frequency is not as high as before, it should contribute more to the bMIMO than in the region B_1. In this case, we should observe a deviation in bMIMO response from the

monochromatic low-frequency response, as observed in figures 3.4 and 3.5 by the region shaded in light green. Further increase of the magnetic field increases the LL separation even more to a situation shown in figure 3.9(a) with a magnetic field of B_3. Here, the order of excitation from the low frequency becomes less than one, and the order of excitation of high frequency approaches 1. In this scenario, low-frequency MW photons' energy is unable to excite electrons to the next LL. Thus we should observe a complete dominancy of the high-frequency monochromatic response in the bMIMO line shape as shown in figure 3.7. This qualitative reasoning provides an intuitive understanding, but we should also consider the MW power into account to further clarify the behavior of the bMIMO system.

3.3 Setup to observe derivative of diagonal resistance

The magnetic field dependency of the bMIMOs should be counted into the account while analyzing the power dependency of the bMIMOs. This is doable due to a significant characteristic of MIMOs.

As described in equation 2.26, the oscillatory diagonal resistance under MW illumination could be fitted into an exponentially damped sinusoidal function, as shown in figure 3.10[10]. All the experimental data points out that the node points occur whenever $B^{-1}/\delta = j$ where $j = 1,2,3,\ldots$ the fitted function is shown in equation 3.3 where λ is the damping factor, and F is the resistance oscillation frequency

$$R_{xx}^{osc} = A' exp\left(\frac{-\lambda}{B}\right) sin\left(\frac{2\pi F}{B} - \pi\right). \tag{3.3}$$

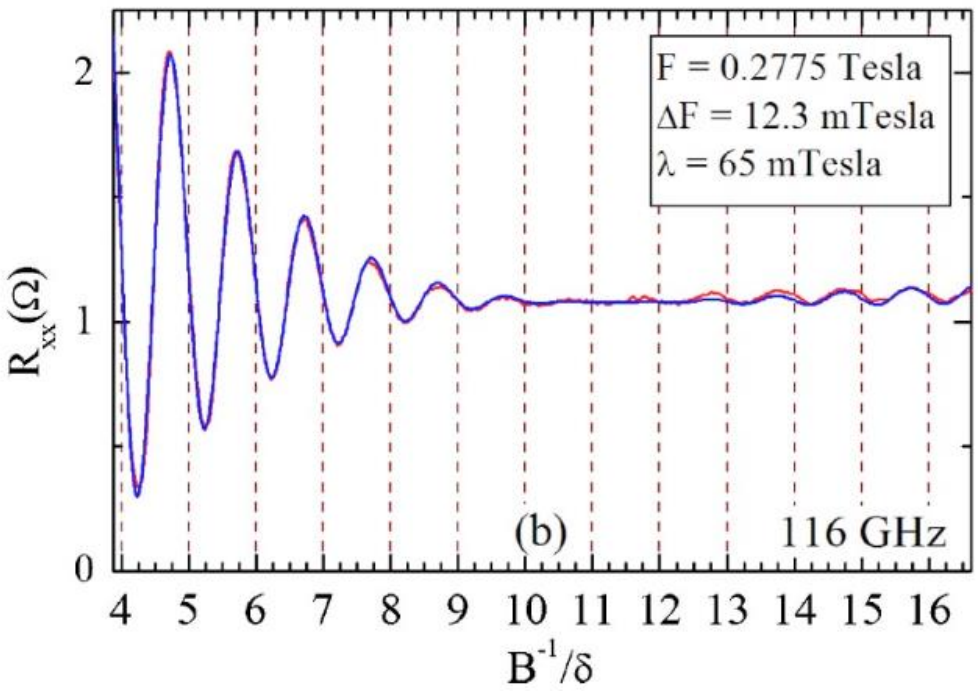

Figure 3.10 Experimental and fitted R_{xx} oscillations at MW frequency 116 GHz [10]. The figure illustrates the periodic nature of MIMOs with the inverse magnetic field. The red and the blue line shows the experimental results and the fitted results respectively obtained for oscillatory diagonal resistance, R_{xx} with respect to B^{-1}/δ, where $\delta = F^{-1}$ in equation 3.3, by Mani et al.

If the monochromatic MIMO harmonic node points (see equation (3.6)) are numbered and plotted with respect to the inverse magnetic field values where they occur, otherwise known as half-cycle plots, we should observe a linear graph. It is evident from the observation that the number of oscillations observed at the temperatures we could achieve is not that high. To overcome this, we could alter our setup to observe the derivative of the diagonal resistance.

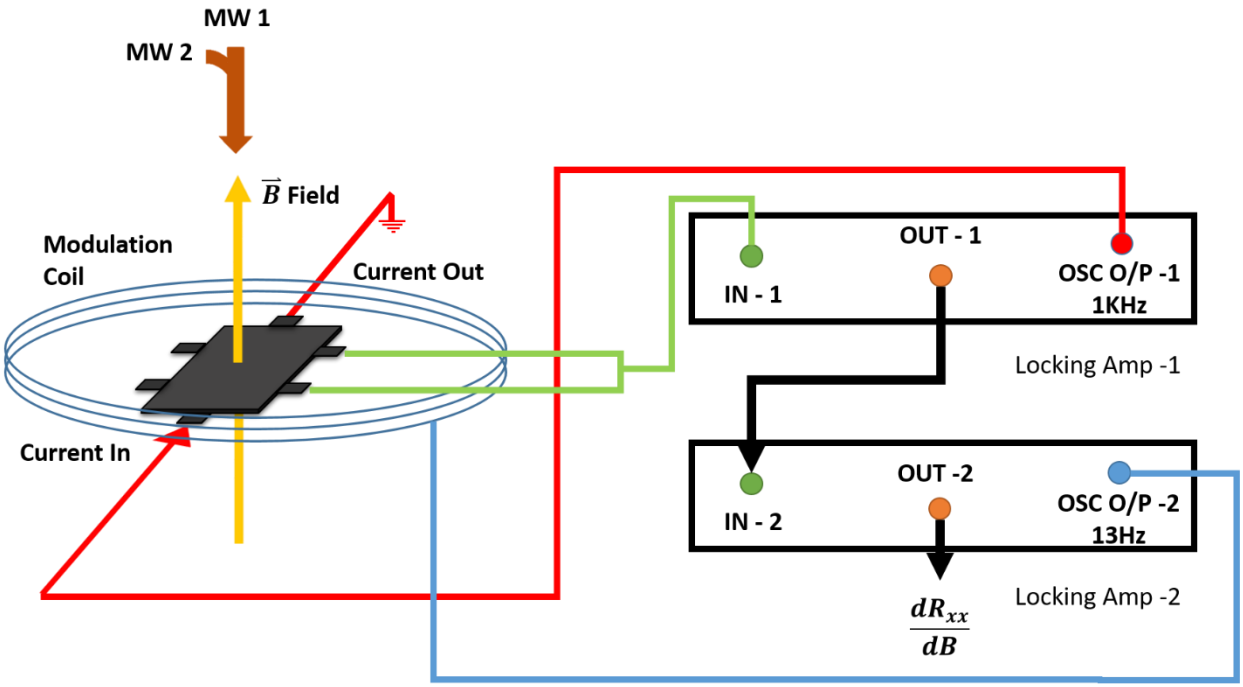

Figure 3.11 Setup to observe the derivative of diagonal resistance under MW irradiation. The B field is applied by a superconducting magnet placed inside the cryostat, as shown in figure 3.1(a). Additionally, a small modulation coil is introduced around the sample, which drives from a Lock-in amplifier at a frequency of 13 Hz. This introduces an additional small magnetic field, δB for the system. Two MW sources were connected to the waveguide coupler at the top of the waveguide. An ac current of frequency 1kHz and 3 μA was driven through the sample using the first Lock-in amp while measuring R_{xx} at 1kHz from the same Lock-in amplifier. The output of the 1st Lock-in amplifier was supplied as the input to the 2nd Lock-in amp, which measures at the frequency of 13 Hz to obtain the derivative of diagonal resistance, dR_{xx}/dB.

Diagonal resistance depends on the magnetic field through the sample. Thus by using Taylor's expansion, an equation could be written for a small change of magnetic field δB as,

$$R_{xx}(B+\delta B) = R_{xx}(B) + \frac{dR_{xx}}{dB}\delta B + \frac{d^2R_{xx}}{dB^2}(\delta B)^2 + \cdots. \tag{3.4}$$

Since the introduced δB from the modulation coil is very small compared to the magnetic field applied to the sample using the superconducting magnet immersed inside liquid He4, higher-order terms in equation (3.4) could be neglected

$$R_{xx}(B + \delta B) = R_{xx}(B) + \frac{dR_{xx}}{dB}\delta B \,. \tag{3.5}$$

Since we are using two Lock-in amplifier system to measure, we could measure the diagonal resistance $R_{xx}(B)$ using the 1st Lock-in amplifier in figure 3.11 at 1kHz frequency. This could be output as the input of the 2nd Lock-in amplifier, which measures at the frequency of modulation coil driven voltage of 13 Hz. Then the output of the second Lock-in amplifier gives us the change of the diagonal resistance with respect to magnetic field change otherwise, the derivative of the diagonal resistance with respect to the magnetic field, dR_{xx}/dB.

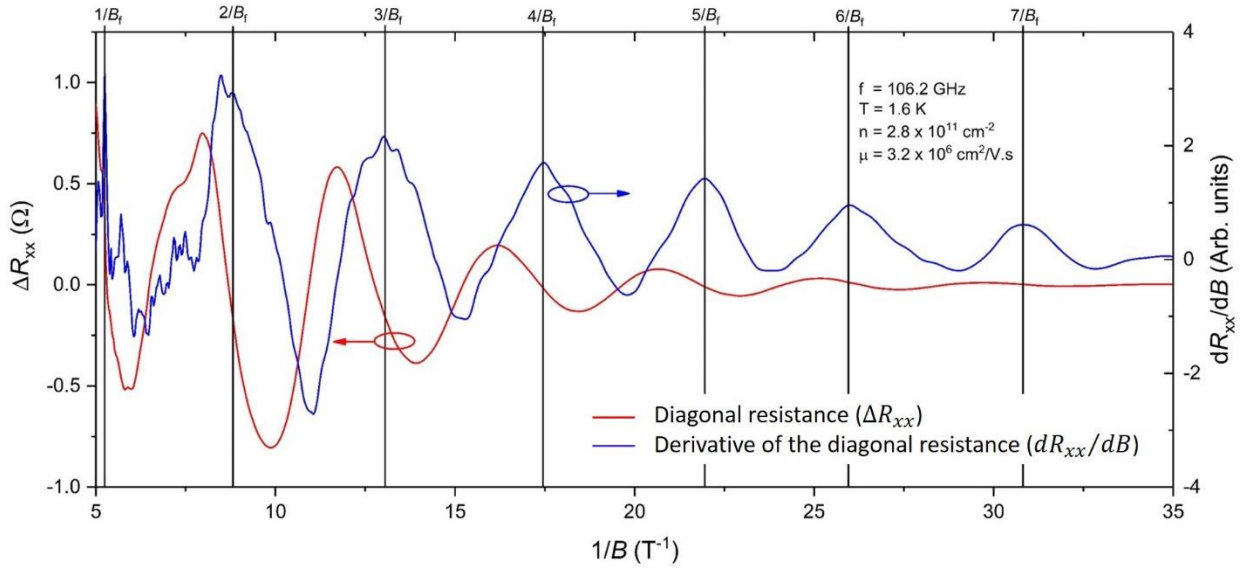

Figure 3.12 Difference of the experimental diagonal resistance from the dark curve(ΔR_{xx}) and the derivative of diagonal resistance(dR_{xx}/dB) with respect to the inverse magnetic field. The diagonal resistance (red line) and the derivative of diagonal resistance (blue line) values are in the left and the right y-axis, respectively. At low magnetic fields, the dR_{xx}/dB shows good oscillatory behavior than ΔR_{xx} because it is more sensitive to the changes in the resistance (i.e., the amplitudes of the dR_{xx}/dB are more pronounced at lower magnetic field regions). In the diagonal resistance signal, the node points correspond to the resonance and harmonics. In the derivative of the diagonal resistance signal, the peaks correspond to the resonance and harmonics of the MW-induced oscillatory resistance (experimental results by Mani and Binuka yet to be published).

It is evident from figure 3.12 that it is easier to observe small changes in oscillatory diagonal resistance using the derivative of the diagonal resistance with respect to the magnetic

field dR_{xx}/dB (blue line)rather than using the change of diagonal resistance from the dark curve ΔR_{xx}(red line).

3.4 bMIMO dependency with MW power

X.L. Lie et al.[2] has done some theoretical work on the experiment performed by M. A. Zudov et al. [5] in 2006. Diving a little into the obtained results provide insight for our experiment under the bichromatic MW irradiation of GaAs/AlGaAs 2DES. Here, they have used photon-assisted scattering-based theory[44, 47, 53, 54] to develop a model for bMIMO observed by the experiment using frequencies 47 and 31 GHz. Their result obtained is shown in figure 3.13

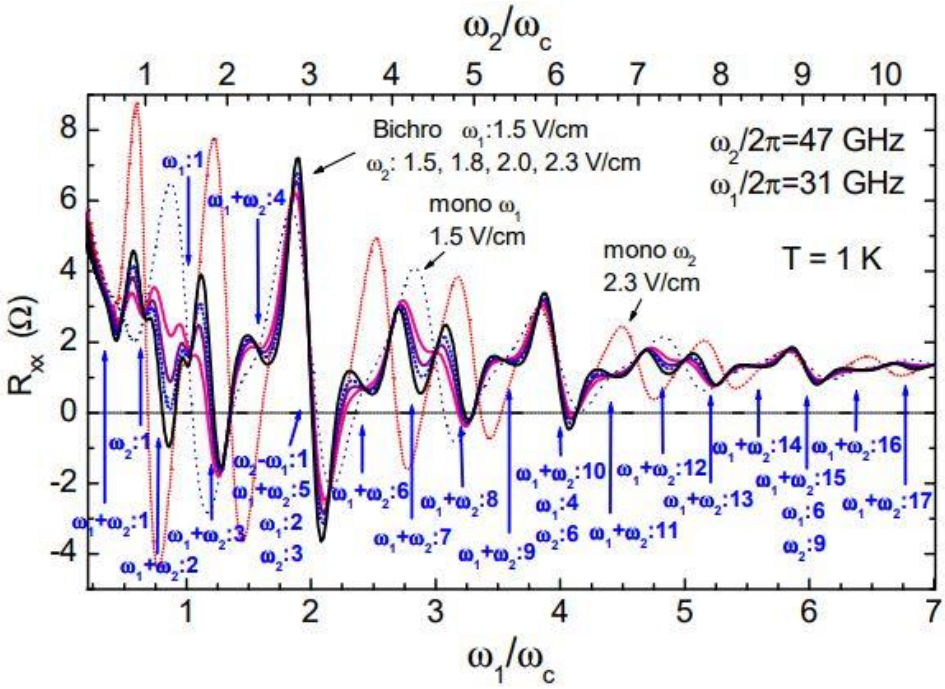

Figure 3.13 Magnetoresistivity R_{xx} induced by bichromatic and monochromatic MW radiations obtained by X. L. Lei et al.[2]. (color online) each node point is labeled with the corresponding frequency of that node. Here the 31 GHz MW was restricted to $1.5\,V/cm$ *while changing the 47 GHz power as* 1.5,1.8,2.0 *and* $2.8\,V/cm$*. Results exhibit the bMIMO lineshape showing the MW frequency response corresponding to* $31\,GHz + 47\,GHz = 78\,GHz$ *for the most part. Blue arrowheads represent the corresponding cyclotron resonance and harmonic node points for indicated frequency.*

It is interesting to see that regardless of the MW power node points remain the same. Thus a half-cycle plot could provide an insight towards the frequency follows by the bMIMO. First of all, we have digitized the data obtained by X. L. Lei et al.[54] and plotted the half-cycle plot for all the monochromatic MIMOs and bMIMO.

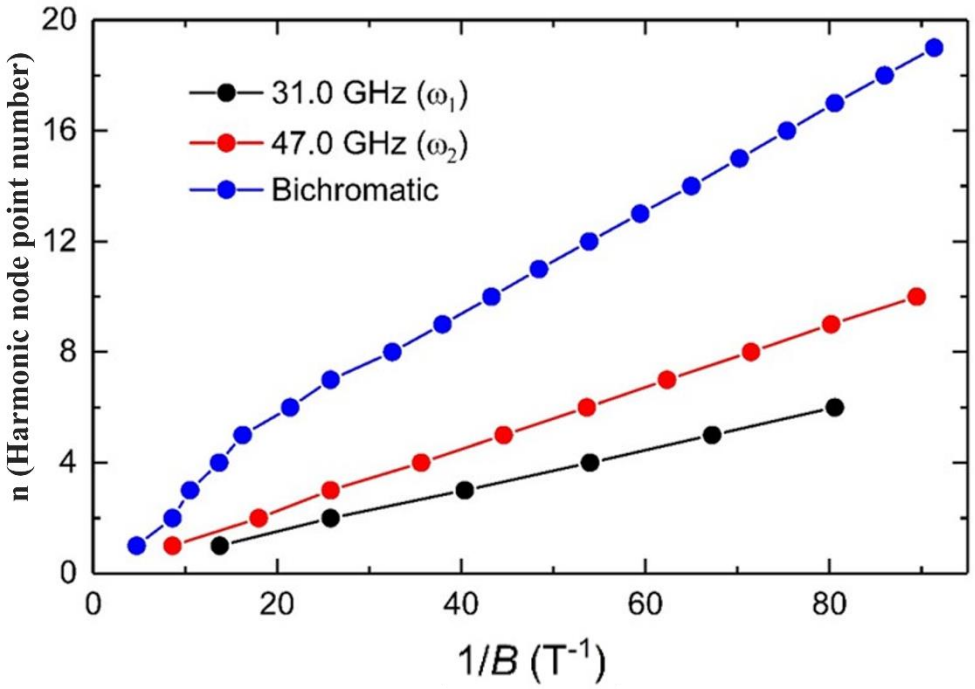

Figure 3.14 Half cycle plot for the data obtained by X. L. Lei et al. for monochromatic and bichromatic MIMOs. Labeled resonance harmonic node points (With blue arrowheads) of figure 3.13 were plotted with the corresponding inverse magnetic field values. The slop of the lines corresponds to the MWs used for the illumination. The Black and red lines show the half-cycle plots for monochromatic MW response of 31.0 GHz and 47.0 GHz, respectively. The blue line shows the half-cycle plot relates to the bMIMO response obtained by X. L. Lei et al.[2] The slope of the blue line is corresponding to the MW frequency of $31\ GHz + 47\ GHz = 78\ GHz$ *or the addition of two monochromatic MWs used for the bichromatic MW.*

The linear relation of the half-cycle plot could be written as shown in equation (3.6). Here n is the harmonic node point number,

$$n = \frac{2\pi f m^*}{e}\frac{1}{B} = \frac{B_f}{B}. \tag{3.6}$$

Thus we could calculate the frequency corresponds to the slop of the half-cycle plot using equation 3.6. Figure 3.14 shows that the bMIMO slop follows neither the slops corresponds to 47.0 GHz

and $31.0\,GHz$. In fact, it follows the slope of frequency $78.0\,GHz$, which is given by $47.0 + 31.0\,GHz$ at a lower magnetic field region.

In our experiment, we have used the dR_{xx}/dB vs. $1/B$ plots to find the node points. In figure 3.12, we could observe that there is a major difference between nodes points in two curves of ΔR_{xx} vs. $1/B$ and dR_{xx}/dB vs. $1/B$. We know that from equation 2.26 that,

$$R_{xx} \sim sin\left(\frac{2\pi B_f}{B}\right). \tag{3.7}$$

In this case, we have node points locate at cyclotron resonance and harmonics otherwise in between an adjacent peak and a valley. But if we observe the curve of dR_{xx}/dB vs. $1/B$

$$\frac{dR_{xx}}{dB} \sim \frac{1}{B^2} cos\left(\frac{2\pi B_f}{B}\right). \tag{3.8}$$

The nodes' points locate at peaks. In figure 3.12, the top x-axis shows the corresponding harmonic resonance for both curves. Figure 3.15 (a) and (b) show the lineshape behavior of the previously considered frequency combination of $90.6\,GHz + 41.0\,GHz$ and $90.6GHz + 48.7\,GHz$, respectively. The figures show only the lineshape of diagonal resistance with the magnetic field while changing the low-frequency MW radiation power systematically from $0.25\,mW$ to $4\,mW$.

In figure 3.15, regions (0), (1), and (2) indicate the regions where we can observe the effect of change of MW power. When the low-frequency power gradually increases, the bMIMO lineshape exhibits monochromatic low-frequency MIMO line features. For instance, in the region (1) in figure 3.15(a), we could identify the peak of the bMIMO changes into a valley when increasing the MW power of low-frequency MW power. Region (3) corresponds with the SdH oscillations. This area should be further analyzed to understand the effect of MWs in that region. It is our understanding that this is governed mostly by the electron heating gained from MW radiation[40] for many experiments we have performed.

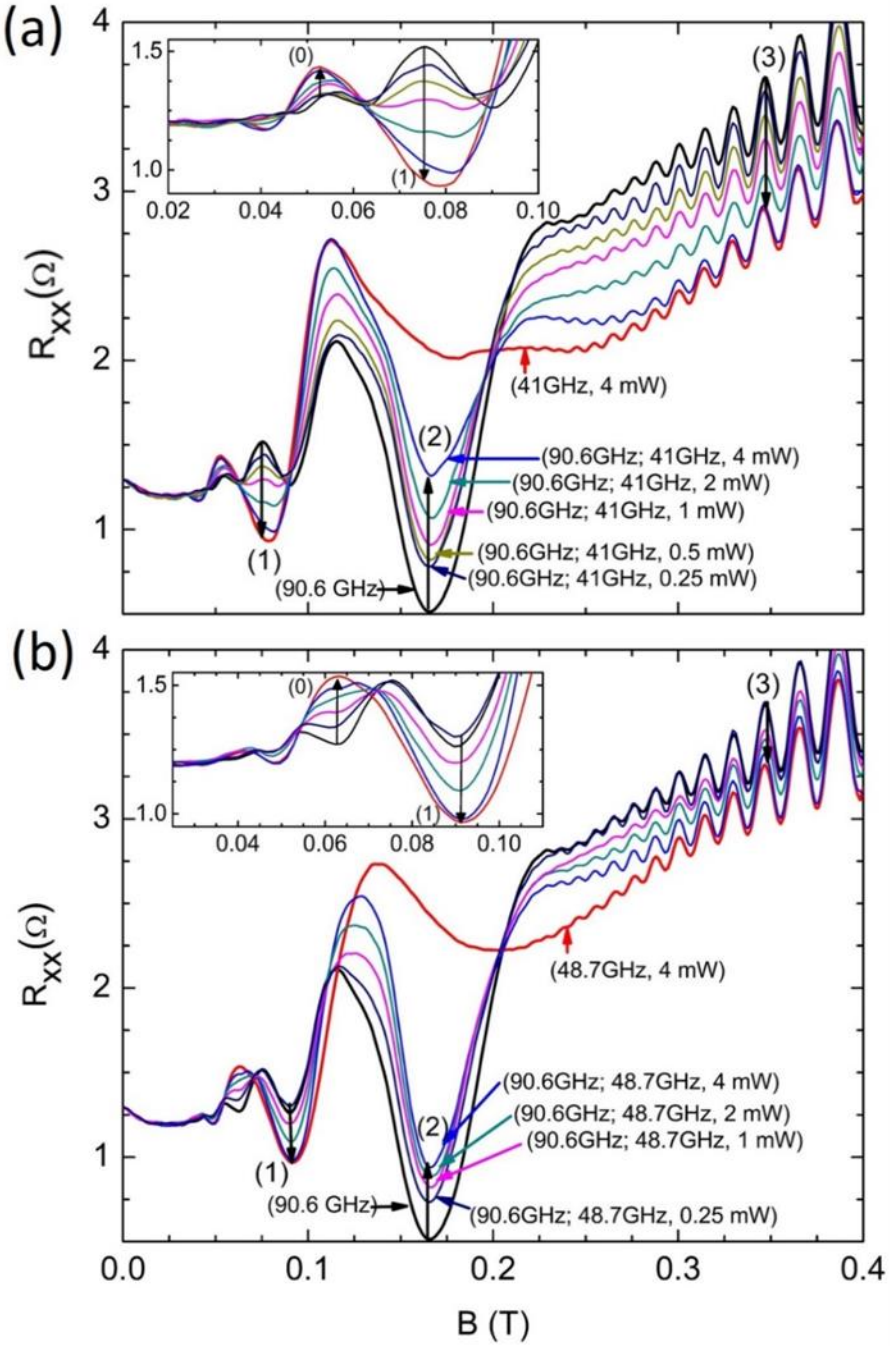

Figure 3.15 Experimental bMIMO and monochromatic MIMO lineshapes corresponding to frequency combinations of (a) 90.6,41.0GHz, Inset: the magnified version of the diagonal resistance line shapes from 0.02 T – 0.1 T. and (b) 90.6, 48.7 GHz, Inset: the magnified version of the diagonal resistance line shapes from 0.02 T – 0.12 T with the systematic low-frequency power variation from 0.25-4 mW[9]. (Color online) region (0), (2), (3), and (4) are labeled to identify and discuss the change of lineshapes of those particular points where peaks and valleys of diagonal resistance line shape coincide. Here the high-frequency MW power was kept at a constant while changing the low-frequency MW power.

Even though figure 3.15 shows the effect of MW power on bMIMO lineshape, the oscillations are not sufficient for the half-cycle plots. Using the two Lock-in amplifiers as mentioned before, the derivative of diagonal resistance was calculated for the frequencies 106.2 GHz, 41.0 GHz, and the bichromatic Mw from the combination. Figure 3.16 shows dR_{xx}/dB vs. $1/B$ plots with the resonance peaks marked on them.

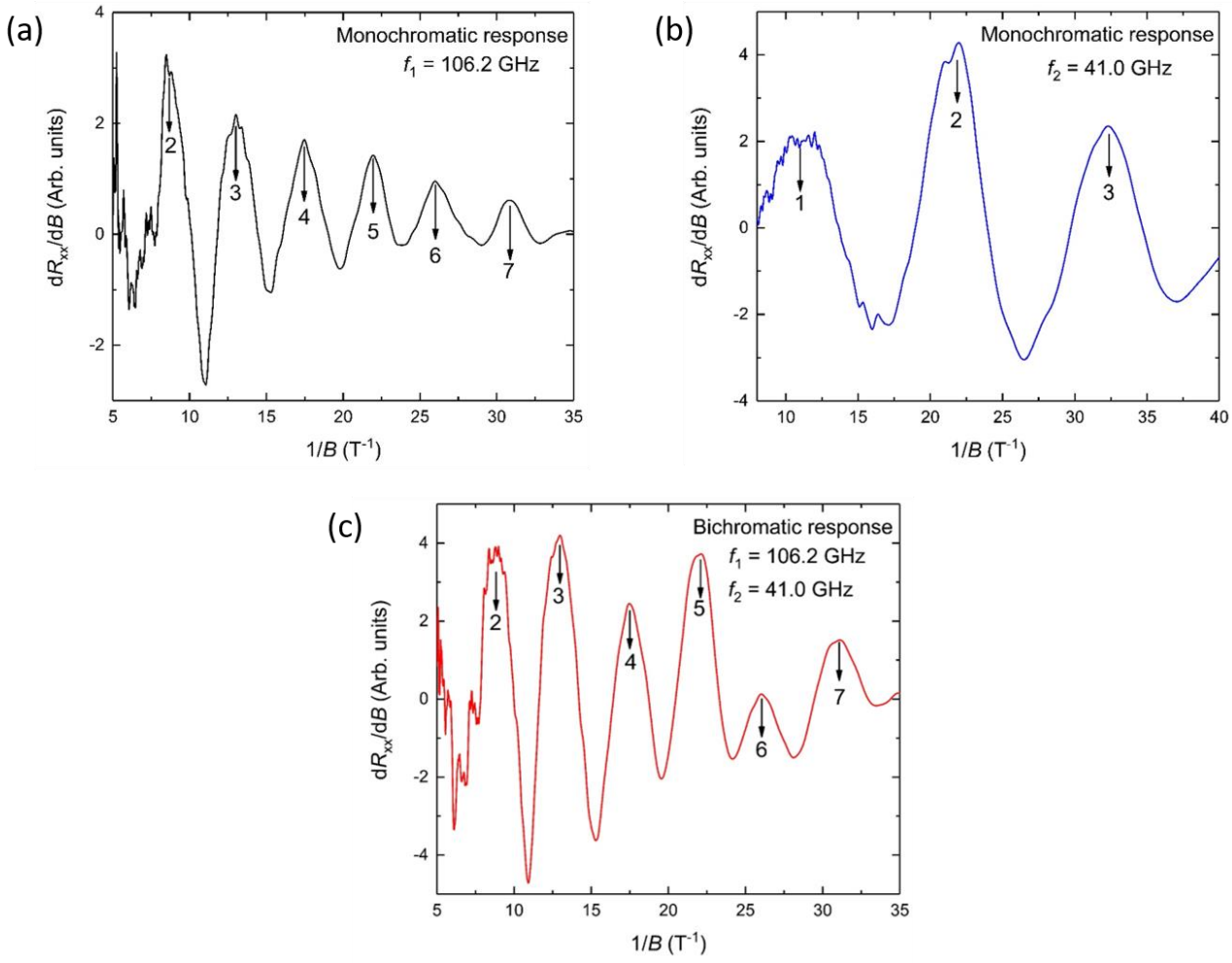

Figure 3.16 Experimental dR_{xx}/dB vs. $1/B$ plots for (a) monochromatic frequency 106.2 GHz, (b) monochromatic frequency 41.0 GHz, and (c) bichromatic frequency of the frequency combination. The derivative of diagonal resistance with the inverse magnetic field. Corresponding cyclotron resonance harmonics are marked on each plot with arrows with corresponding harmonic numbers evaluated using equation 3.6. The results were later used in figure 3.17 to plot the half-cycle plots for the monochromatic and bichromatic MW response (experimental results by Mani and Binuka yet to be published).

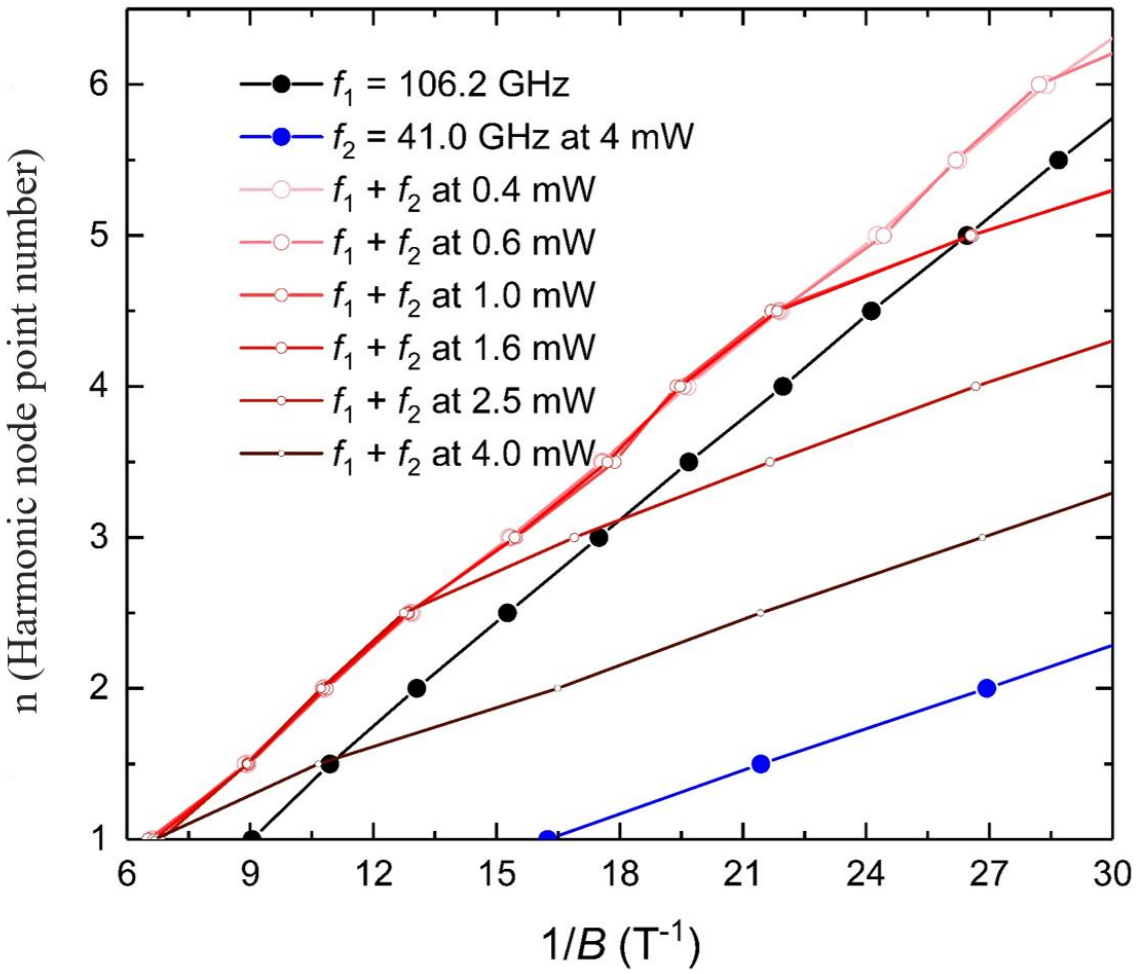

Figure 3.17 Half cycle plots for frequencies 106.2 GHz, 41.0 GHz and the bichromatic MW of the two frequency combination with systematic MW power change of low-frequency 41.0 GHz calculated using the experimental results. (Color online). Different Bichromatic MWs were used to irradiate the sample by varying MW power of low-frequency (f_2) from 0.4 mW to 4.0 mW. The blue and black lines show the half-cycle plot corresponds to monochromatic MWs of 41.0 GHz and 106.2 GHz. The bichromatic diagonal resistance lineshape follows either the high frequency or low-frequency monochromatic slopes depending on the strength of the magnetic field applied. This suggests that the line shape of bMIMO only follows two monochromatic responses for the particular magnetic field considered. The half-cycle plot of bMIMO changes its slope at different magnetic fields while changing the MW power of low monochromatic. This suggests that the MW power is determining the dominant monochromatic MW response (Calculated result by Mani and Binuka yet to be published).

As shown in the figure, we can see the linear lines we obtain for the two monochromatic MIMO half-cycle plots. The bMIMO half-cycle plots follow the low-frequency response at low

magnetic field regions, hence having the same slope as the low-frequency monochromatic response. As the magnetic field increases, the bMIMO half-cycle plot starts to follow the high-frequency monochromatic half-cycle slope indicating the previously explained magnetic field dependency of bMIMOs. At the same time, we could observe that the turning point of the bMIMO half-cycle plots from monochromatic low-frequency slope to that of high-frequency changes with the increment of low-frequency power. When the MW power of low-frequency increases, the bMIMO starts to exhibit or follow more of the monochromatic low-frequency MIMO response. Interesting, in our experiment, we did not observe any line slopes of bMIMO corresponding to the addition of MW ($f_1 + f_2$) of the difference of MWs ($f_1 - f_2$) used to the bichromatic illumination as in the simulation done by X. L. Lei[2].

4 RADIATION DRIVEN ORBIT MODEL FOR MIMOS

Here we would like to dive more into the radiation-driven orbit model for MIMOs suggested by J. Iñarrea et al. [3] and using the experimental [9, 41] and simulated data to understand the bMIMO behavior by further developing the radiation driven orbit model for bichromatic MW illumination.

4.1 More on Landau Levels

As described earlier, electrons in a magnetic field follow circular paths due to the Lorentz force. Those circular paths are quantized, resulting in discrete Landau levels (LLs). Interestingly the LLs were first observed in 3D materials, where the electron circular orbits are formed in a plane perpendicular to the applied magnetic field. Below we disregard the effects related to the electron spin. In a magnetic field, Zeeman energy splitting for an electron with spin up and down is given by $\Delta = 2\mu_B B$ where $\mu_B = e\hbar/2m$ is the Bohr magnetron. If the magnetic field is low enough, electrons are effectively spinless. The Lagrangian of an electron moving in a magnetic field $\boldsymbol{B} = \boldsymbol{\nabla} \times \boldsymbol{A}$ could be written as

$$L = \frac{1}{2} m\dot{\boldsymbol{x}}^2 - e\dot{\boldsymbol{x}}.\boldsymbol{A}\,. \tag{4.1}$$

The corresponding canonical momentum has the following form

$$\boldsymbol{p} = \frac{\partial L}{\partial \dot{x}} = m\dot{\boldsymbol{x}} - e\boldsymbol{A}\,. \tag{4.2}$$

Then the Hamiltonian is

$$H = \dot{\boldsymbol{x}} \cdot \boldsymbol{p} - L = \frac{1}{2m}(\boldsymbol{p} - e\boldsymbol{A})^2\,. \tag{4.3}$$

The Hamiltonian in terms of a mechanical momentum is $H = m\dot{\boldsymbol{x}}^{\boldsymbol{2}}/2$. From this expression, it looks like the magnetic field does not affect the system.

But if we consider the Poisson brackets of mechanical momentum with itself, it is not vanishing and is proportional to the magnetic field,

$$\{m\dot{x}_i, m\dot{x}_j\} = \{p_i - eA_i, p_j - eA_j\} = -e\left(\frac{\partial A_j}{\partial x_i} - \frac{\partial A_i}{\partial x_j}\right) = -e\epsilon_{ijk}B_k \,. \tag{4.4}$$

Let's introduce a new expression for mechanical momentum, which is called generalized momentum, as

$$\boldsymbol{\eta} = \boldsymbol{p} - e\boldsymbol{A} = m\dot{\boldsymbol{x}} \,. \tag{4.5}$$

For generalized momentum, the communication relation (the commutator is proportional to the corresponding Poisson bracket) is

$$[\eta_x, \eta_y] = -ie\hbar B \,. \tag{4.6}$$

Now we could introduce a lowering and a rasing operator as follows

$a = \frac{1}{\sqrt{2e\hbar B}}(\eta_x - i\eta_y)$ and $a^\dagger = \frac{1}{\sqrt{2e\hbar B}}(\eta_x + i\eta_y)$.

so that $[a, a^\dagger] = 1$, then the Hamiltonian (4.3) could have written as

$$H = \frac{1}{2m}\boldsymbol{\eta}\cdot\boldsymbol{\eta} = \hbar\omega_c\left(a^\dagger a + \frac{1}{2}\right). \tag{4.7}$$

The Hamiltonian (4.7) is similar to the Hamiltonian of the quantum harmonic oscillator. Then the corresponding quantum state $|n\rangle$ has energy spectrum

$$E_n = \hbar\omega_c\left(n + \frac{1}{2}\right). \tag{4.8}$$

To find the eigenstates, we need to specify a gauge potential. We choose the Landau gauge with vector potential $\boldsymbol{A} = xB\hat{\boldsymbol{y}}$. Here the magnetic field is invariant under the translational symmetry, while $\boldsymbol{A}$ is not. Vector potential $\boldsymbol{A}$ breaks translational symmetry in x direction but not in y direction. In this case, the Hamiltonian becomes

$$H = \frac{1}{2m}\left(p_x^2 + \left(p_y - eBx\right)^2\right). \tag{4.9}$$

Because of the translational invariance along the y direction, eigenstates of the system have the form

$$\Psi_k(x,y) = e^{iky} f_k(x). \tag{4.10}$$

Substituting this expression into equation (4.9), we obtain

$$\begin{aligned} H\Psi_k(x,y) &= \frac{1}{2m}(p_x^2 + (\hbar k - eBx)^2)\Psi_k(x,y) = H_k\Psi_k(x,y). \\ H_k &= \frac{1}{2m}p_x^2 + \frac{m\omega_c^2}{2}(x + kl_B^2)^2). \end{aligned} \tag{4.11}$$

This is the same Hamiltonian as the one for a harmonic oscillator displaced from the origin and centered at $x = -kl_B^2$. Here $l_B = \sqrt{\hbar/eB}$ is the magnetic length. Now the wave function depends on two quantum numbers $n \in \mathbb{N}$ and $k \in \mathbb{R}$. The energy of the LLs depends only on n, but LL becomes highly degenerate due to the quantum number k. For example, consider a rectangular sample with side lengths L_x and L_y. Because the wavefunctions are exponentially localized at $x = -kl_B^2$, for a finite sample with length $0 \le x \le L_x$, k values should be in the range of $-L_x/l_B^2 \le k \le 0$. So the number of degenerated states, or the degeneracy, N is

$$N = \frac{L_y}{2\pi}\int_{-L_x/l_B^2}^{0} dk = \frac{L_x L_y}{2\pi l_B^2} \Longrightarrow k = \frac{2\pi}{L_x}N. \tag{4.12}$$

The degeneracy of the LL is very important for many quantum phenomena, including the MIMOs.

4.2 The theory behind radiation driven orbit model

The LL orbits discussed in the previous section are geometrically fixed within the sample. The radiation-driven orbit model suggests that when the 2DES is illuminated with MWs, the LL orbits start oscillating. Then we can solve the dynamics of such oscillations using the wave equation and a solution for forced oscillators suggested by Edward H. Kerner [55] in 1958.

MW radiation is introduced as a time-varying external electric force acting on a 2DES subjected to a magnetic field. Using Edward H. Kerner's solution and applying it to MW irradiated 2DES, K. Park [56] had derived the corresponding solution as follows. We assume that the radiation wavelength is long enough so that the electric field is uniform over the sample. Choosing the Landau gauge, $\boldsymbol{A} = B(0, x)$, where the momentum in the y direction (k is a good quantum number) and with $k = -X_j/l_B^2$ (l_B – magnetic length), the single particle Hamiltonian could be written as

$$H = \frac{P_x^2}{2m} + \frac{1}{2}m\omega_c^2\left(x - X_j\right)^2 - F(t)\left(x - X_j\right) - F(t)X_j = H_F\left(P_x, x - X_j\right) - F(t)X_j\,. \qquad (4.13)$$

where, $F(t) = eEcos(\omega t)$, E is the electric field and $H_F(P_x, x)$ is the Hamiltonian of time-independent forced harmonic oscillator centered at $x = X_j$. Time-dependent forced harmonic oscillator, described by $H_F(P_x, x)$, has an analytical solution of the form

$$\Psi(x, t) = \chi(x - x_{cl}(t), t)e^{i\theta t}\,. \qquad (4.14)$$

where

$$\theta(x, t) = \frac{m}{\hbar}\frac{dx_{cl}(t)}{dt}\left(x - x_{cl}(t)\right) + \frac{1}{\hbar}\int_0^t L dt'\,. \qquad (4.15)$$

Here $\chi(x, t)$ satisfy the Schrodinger equation of the unforced harmonic oscillator. The center position of the orbits $x_{cl}(t)$ satisfy the classical motion of the forced harmonic oscillator $m(d^2x_{cl}(t)/dt^2) + m\omega_c^2 x_{cl}(t) = F(t)$ with the solution given by the following expression

$$x_{cl}(t) = \frac{eE_{ac}}{m\sqrt{(\omega_c^2 - \omega^2)^2 + \gamma^4}}\cos\omega t\,. \qquad (4.16)$$

Here γ is a phenomenological damping factor [3]. Also, L is the classical Lagrangian

$$L = \frac{m}{2}\left(\frac{dx_{cl}(t)}{dt}\right)^2 - \frac{m\omega_c^2}{2}x_{cl}(t)^2 + F(t)x_{cl}(t)\,. \qquad (4.17)$$

Then the wavefunction (4.14) takes the following form

$$\Psi(x,t) = \chi_n\big(x - X_j - x_{cl}(t), t\big)e^{i\theta(x,t)} \times exp\left(\frac{i}{\hbar}X_j\left\{\int_0^t F(t')dt' - m\frac{dx_{cl}(t)}{dt}\right\}\right). \qquad (4.18)$$

Here χ_n is the solution of the Schrodinger equation of the unforced quantum harmonic oscillator. The energy is not conserved under the irradiation, but the LL indexing is a good quantum number. The orbital part of the solution in equation (4.18) is quantized in the same way as eigenstates without the MW radiation. The density of states is also the same as without radiation. The equation (4.18) could also be rewritten as follows

$$\Psi(x,t) = \chi_n\big(x - X_j - x_{cl}(t), t\big)e^{i\theta(x,t)} \times \sum_{m=-\infty}^{\infty} J_m\left[\frac{eE_{ac}}{\hbar}X_j\left(\frac{1}{\omega} + \frac{\omega}{\sqrt{(\omega_c^2 - \omega^2)^2 + \gamma^4}}\right)\right]e^{im\omega t}. \qquad (4.19)$$

where Jacobi-Anger expansion $e^{iz\sin\emptyset} = \sum_m J_m(z)e^{imz}$ is used. Note that function $\theta(x,t)$ is independent on the center of orbit coordinate X_j. Now we need to introduce the impurity scattering [57], which determines the conductivity of the system. If scattering is weak, time-dependent first-order perturbation theory can be applied to find the corresponding transition rate, $W_{m,n}$, from initial $\Psi_m(x,t)$ to final $\Psi_n(x,t)$ states,

$$W_{m,n} = \lim_{\alpha\to 0}\frac{d}{dt}\left|\frac{1}{i\hbar}\int_{-\infty}^{t'}\langle\Psi_n(x,t)|V_s|\Psi_m(x,t)\rangle e^{\alpha t}dt\right|^2. \qquad (4.20)$$

The scattering potential is $V_s = \sum_q \frac{e^2}{2S\epsilon(q+q_s)}e^{i\vec{q}.\vec{r}}$ [14], where S is the surface of the sample and q_s is the Thomas-Fermi screening constant. Finally, using the expression (4.19) we obtain the following expression for the transmission rate [3]

$$W_{m,n} = \frac{e^5 n_i S}{16\pi^2 \hbar^2 \epsilon^2} B \times \left[\frac{\Gamma}{[\hbar\omega_c(n-m)]^2 + \Gamma^2}\right]$$

$$\times \int_0^{q_{max}} dq \frac{\mathrm{q}}{(q^2+q_0^2)^2} \frac{n_1!}{n_2!} e^{-\frac{1}{2}q^2R^2} \left(\frac{1}{2}q^2 l_B^2\right)^{n_1-n_2} \left[L_{n_2}^{n_1-n_2}\left(\frac{1}{2}q^2 l_B^2\right)\right]^2 \quad (4.21)$$

$$[J_0(A_m^\omega)]^2 [J_0(A_n^\omega)]^2 .$$

where

$$A_{m(n)}^\omega = \frac{eE_{ac}}{\hbar} X_{m(n)} \left(\frac{1}{\omega_1} + \frac{\omega_1}{\sqrt{(\omega_c^2 - \omega_1^2)^2 + \gamma^4}}\right). \quad (4.22)$$

$$X_{m(n)} = \frac{\hbar k_{m(n)}}{eB} - \frac{eE_{dc}}{m_e \omega_c}. \quad (4.23)$$

Here Γ is the LL broadening, $L_{n_2}^{n_1-n_2}\left(\frac{1}{2}q^2 l_B^2\right)$ are associated Laguerre polynomials, $n_1 = \max(n,m)$ and $n_2 = \min(n,m)$. Without the radiation, an electron in state Ψ_m with the center of orbit X_m, is scattered to Ψ_n state with the center of orbit X_n. The corresponding change of electron coordinate during scattering is

$$\begin{aligned} &\mathrm{q} l_B^2 \cos\theta = X_n - X_m = \Delta X_0 . \\ &\mathrm{q}\cos\theta = k_n - k_m . \end{aligned} \quad (4.24)$$

Here the polar coordinates, q, and θ, were used. According to the model, with MW radiation, the electron jumps a distance of $\Delta X(t) = \Delta X_0 + x_{cl}(t)$. It means that the electron orbit center positions oscillate back and forth in x direction under irradiation according to $x_{cl}(t)$. When an electron suffers a scattering process with the probability given by $W_{m,n}$ it takes $\tau_{m,n} = 1/W_{m,n}$ time for that electron to jump from one orbit to another. Then we can write the average coordinate change along the x direction as follows

$$\Delta X(t) = \Delta X_0 + x_{cl}(\tau_{m,n}) = \Delta X_0 + \frac{eE_{ac}}{m\sqrt{(\omega_c^2 - \omega^2)^2 + \gamma^4}} \cos\omega\tau_{m,n} . \quad (4.25)$$

The conductivity then either increases or decreases as described in section 2.8.4, producing MIMOs as shown in figure 4.1. By applying Boltzmann transport theory, the diagonal resistance could be calculated from the following expression [9]

$$R_{xx} \propto \int dE \frac{\left(\Delta X(t)\right)^2}{\tau_{m,n}}. \tag{4.26}$$

where E is the electron energy.

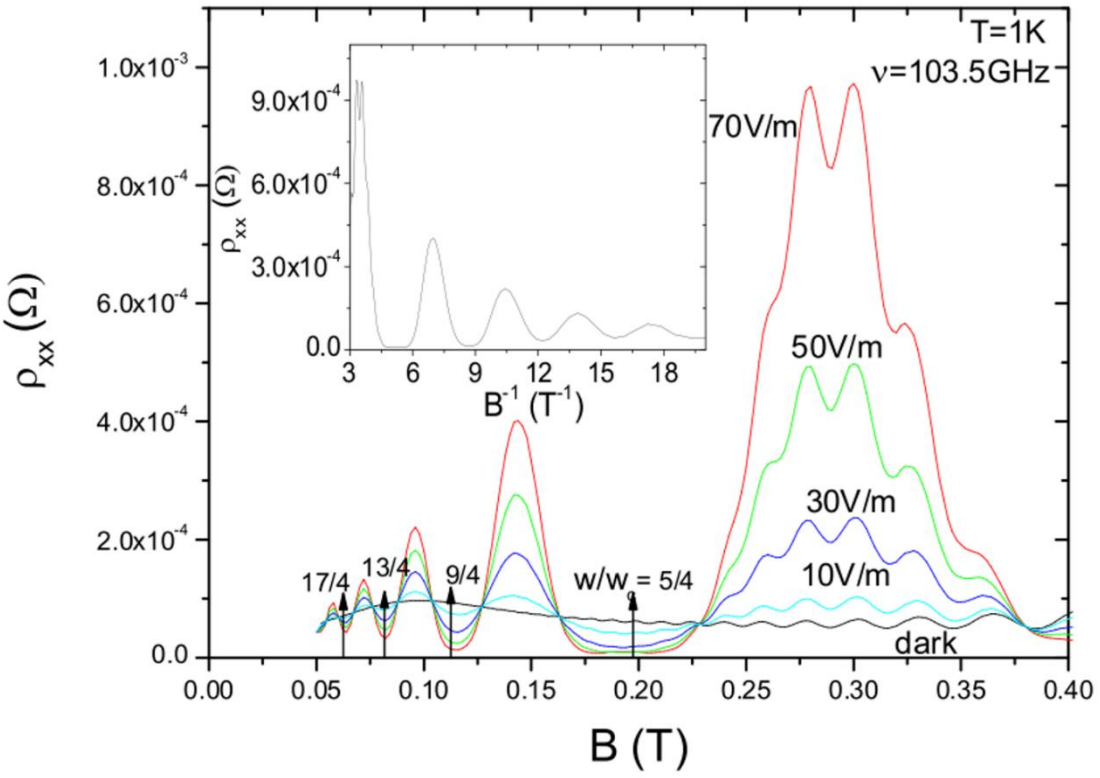

Figure 4.1 Simulated magnetoresistivity as a function of the magnetic field from the radiation-driven electron orbital model by J. Iñarrea et al.[3]. Calculated magnetoresistivity ρ_{xx} as a function of B, for different MW intensities for the MW frequency of 103.5 GHz at MW powers 70V/m (red line), 50V/m (green line), 30V/m (dark blue line) and 10V/m (light blue line). The black line corresponds to the case without radiation. The inset shows ρ_{xx} vs. $1/B$, which is roughly periodic with the inverse magnetic field.

4.3 Radiation Driven orbital model for bMIMOs

For bMIMOs, we have two different frequencies $\omega_1 = 2\pi f_1$ and $\omega_2 = 2\pi f_2$. We could find the transition rates for both high and low frequencies $W_{m,n}^{f_1}$ and $W_{m,n}^{f_2}$ using equation (4.21), which leads to the $\tau_{m,n}^{f_1}$ and $\tau_{m,n}^{f_2}$. Both frequencies drive the guiding center by two different time-dependent sinusoidal forces with two different amplitudes giving rise to interference effects. Then the average distance is

$$\Delta X_{f_1}(t) + \Delta X_{f_2}(t)$$

$$= \left(\Delta X_0^{f_1} + \frac{eE_{ac}^{f_1}}{m\sqrt{(\omega_c^2 - {\omega_1}^2)^2 + {\gamma_{f_1}}^4}} \cos \omega \tau_{m,n}^{f_1} \right) \tag{4.25}$$

$$+ \left(\Delta X_0^{f_2} + \frac{eE_{ac}^{f_2}}{m\sqrt{(\omega_c^2 - {\omega_2}^2)^2 + {\gamma_{f_2}}^4}} \cos \omega \tau_{m,n}^{f_2} \right).$$

The corresponding longitudinal magnetoresistance is given by[9]

$$R_{xx} \propto \int dE \frac{\left(\Delta X_{f_1}(t) + \Delta X_{f_2}(t)\right)^2}{\tau_{m,n}}. \tag{4.28}$$

Here,

$$\frac{1}{\tau_{m,n}} = \frac{1}{\tau_{m,n}^{f_1}} + \frac{1}{\tau_{m,n}^{f_2}}. \tag{4.29}$$

Figure 4.2 shows the experimental and simulated result obtained for the diagonal resistance lineshapes of the bMIMO response for the frequency combination of 90.6 GHz and 48.7 GHz. Both experimental and simulated lines show similar behavior with the positions of the maxima and minima approximately at the same magnetic fields for B less than 0.25 T. There is a large deviation between experimental and simulated results at small magnetic fields, B<0.05 T, which

can be attributed to extra scattering channels in the experimental samples. Although the positions of the main maxima and minima (at B around 0.1 T) of the simulated line are also a little bit shifted from the experimental results, this model still provides the best fit to the experimental data. Extra improvement can be made by considering higher-order processes while describing the scattering events.

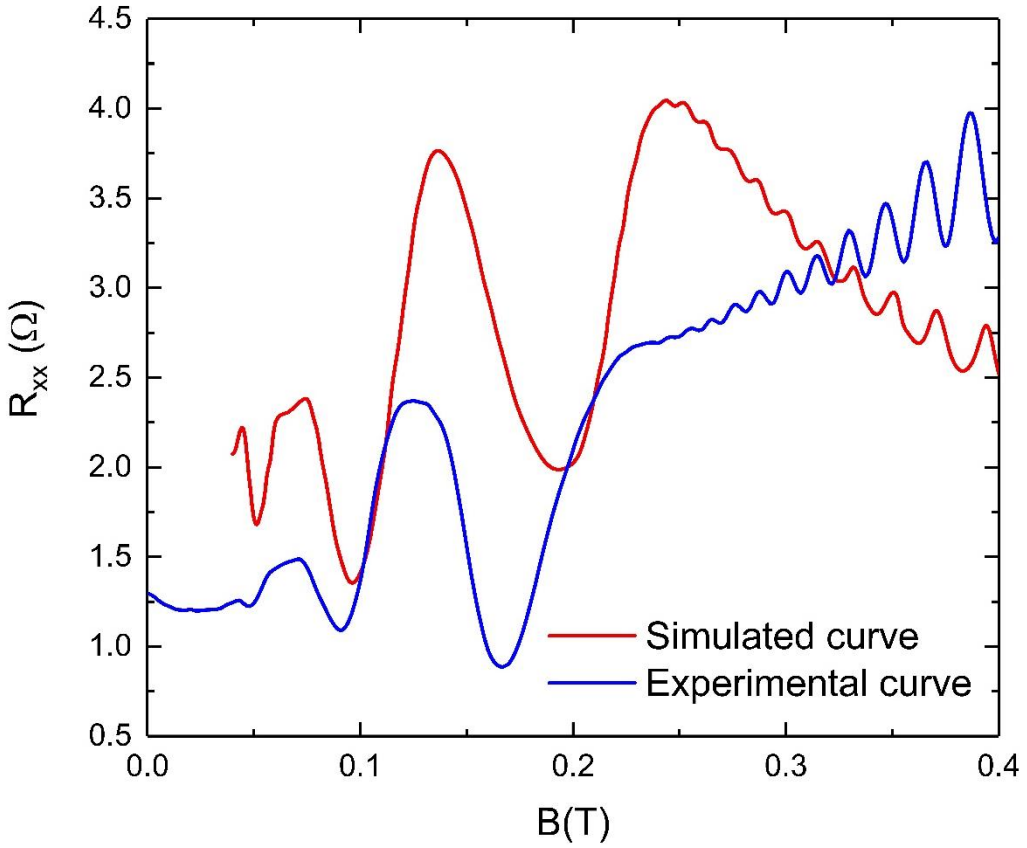

Figure 4.2 Experimental results for bMIMO response of 90.6 GHz and 48.7 GHz (blue line) and the simulated bMIMO response (red line). Although there are some differences in the diagonal resistance values, lineshapes exhibit a similar pattern. The difference in the experimental curve is believed to be due to extra scattering channels in experimental systems (obtained from ref [9]).

Two monochromatic MW responses with MW frequencies of 90.6 GHz and 48.7 GHz and the corresponding bichromatic MW response from the combination were simulated using the model. Figure 4.3 shows the results, where the magnetoresistance is plotted as a function of the inverse magnetic field. The arithmetic average of two monochromatic MW responses and the

simulated result were compared by subtracting the average from the simulated bMIMO response. This produces a similar result as observed experimentally in figure 3.8. Here the same power was used for both MWs. Resistance values of the simulated results are different than the experiment, while resistance difference lineshape in figure 4.3(a) is similar to that of figure 3.8(a).

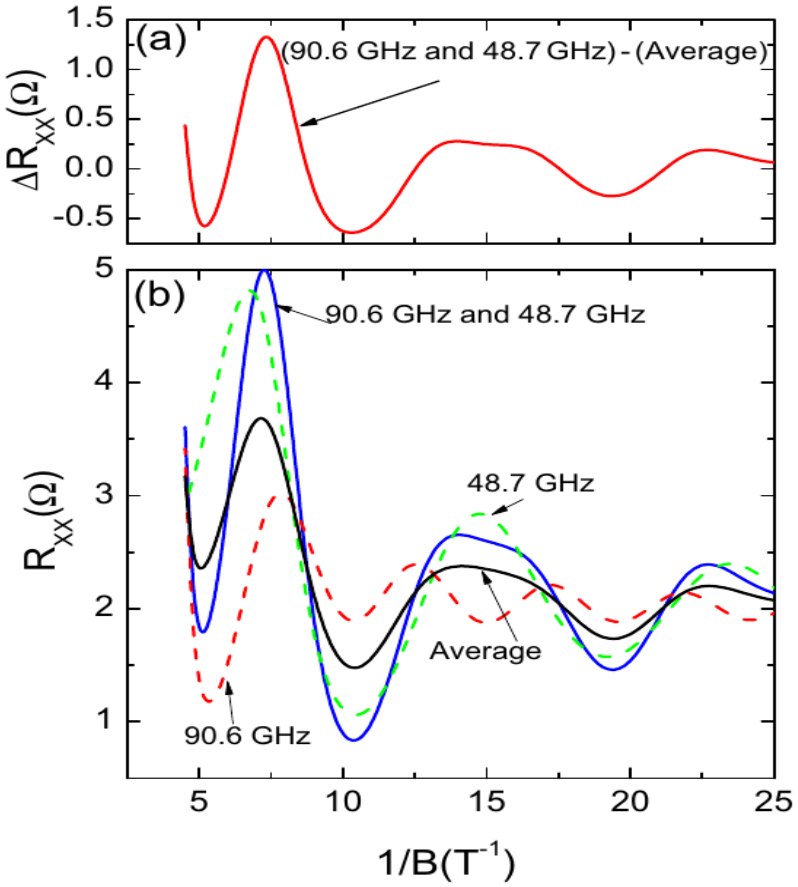

Figure 4.3 The simulated monochromatic and bichromatic diagonal resistance for MW frequencies of 90.6 GHz and 48.7 GHz and the arithmetic average of two monochromatic response with simulated bMIMO response[9]. (a) The difference of the simulated bMIMO response for frequency combination of 90.6 GHz and 48.7 GHz with the arithmetic average of the two monochromatic MIMO responses (red line). (b) The simulated monochromatic MIMO responses for MW frequency 90.6 GHz (dashed red line), 48.7 GHz (dashed green line), bMIMO (solid blue line) and the arithmetic average (solid black line) of two monochromatic responses. Although having different resistance values, the line shape obtained shows similarity to the experimental data obtained in figure 3.8.

Next, we have changed the MW powers of the MWs and simulated the bMIMO lineshapes to observe the corresponding changes in the diagonal magnetoresistance lineshape. The experimental dependences for the frequencies used earlier in figure 3.15 agree reasonably with the simulated data shown in figure 4.4. The two regions labeled as (1) and (2) are shown in the simulated data plots. Diagonal resistance lineshapes at those regions act similar to the experimentally observed lineshapes when the low-frequency MW power increases. The simulated data support the experimental observation that the monochromatic low-frequency response is dominating in the low magnetic field region, and the monochromatic high-frequency response is dominating in the high magnetic field region. The simulation data also suggest that this is mainly due to the effect of the denominator of $A_{m(n)}^{\omega_1}$ and $A_{m(n)}^{\omega_2}$,

$$A_{m(n)}^{\omega_1} = \frac{eE_{ac}^{\omega_1}}{\hbar} X_{m(n)} \left(\frac{1}{\omega_1} + \frac{\omega_1}{\sqrt{(\omega_c^2 - \omega_1^2)^2 + \gamma_1^4}} \right),$$
$$A_{m(n)}^{\omega_2} = \frac{eE_{ac}^{\omega_2}}{\hbar} X_{m(n)} \left(\frac{1}{\omega_2} + \frac{\omega_2}{\sqrt{(\omega_c^2 - \omega_2^2)^2 + \gamma_2^4}} \right). \quad (4.30)$$

The idea is that when the magnetic field increases beyond the corresponding resonance, the damping of the MIMO for that frequency becomes strong. When $f_2 < f_1$ the damping of f_2 (or the low frequency) response is strong while the high frequency f_1 response becomes dominant. On the other hand, at lower magnetic fields $A_{m(n)}^{\omega_2} \gg A_{m(n)}^{\omega_1}$ and with the increase of the MW power, the low-frequency response dominates the low magnetic field region. In between, we could observe a transition region of bMIMO line shape between the low-frequency and the high-frequency monochromatic response.

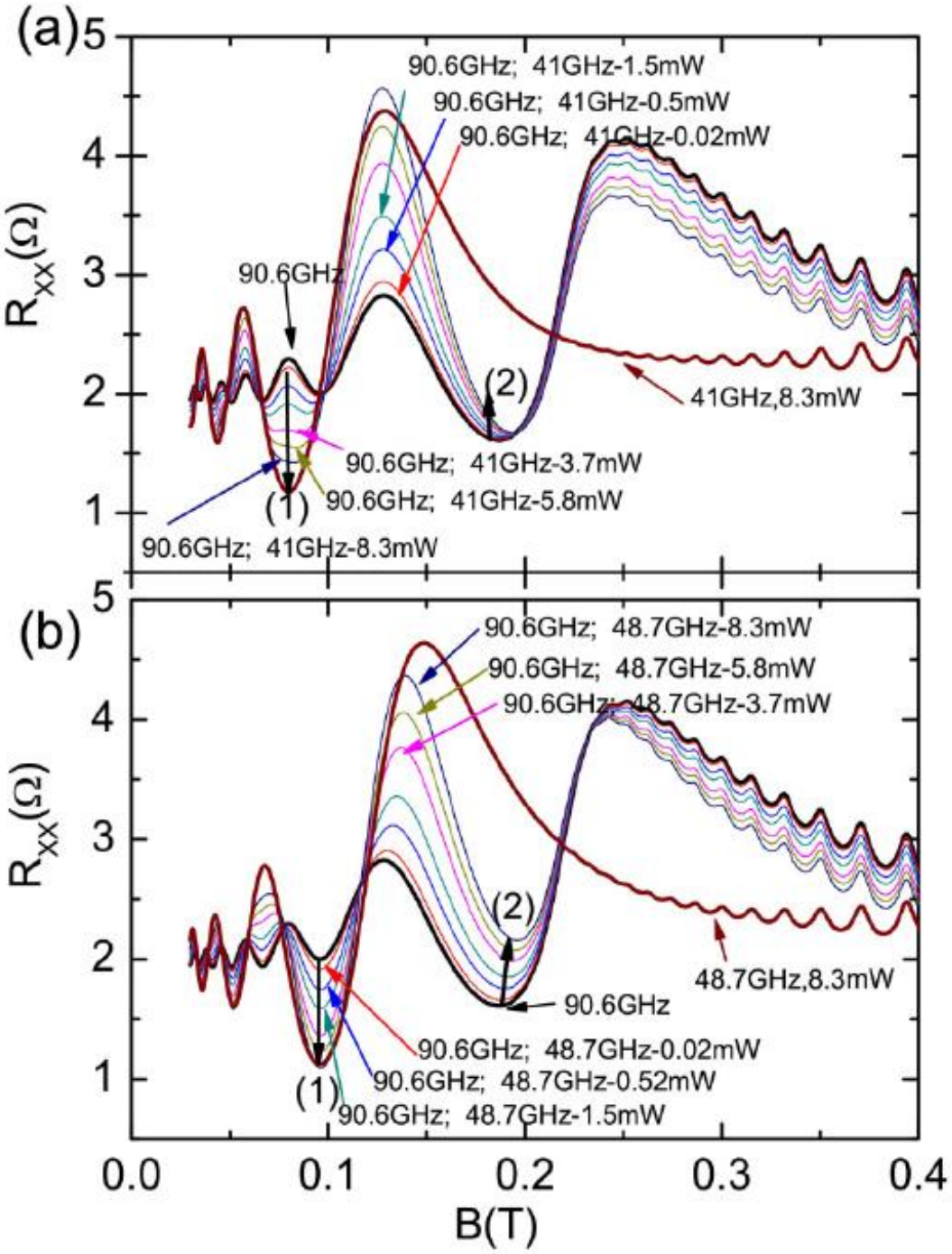

Figure 4.4 Simulated Diagonal resistance vs. the magnetic field data according to the radiation driven orbital model for bichromatic MWs(color online) for frequency combinations of (a) 90.6 GHz and 41.0 GHz (b) 90.6 GHz and 48.7 GHz for different low-frequency MW powers[9]. The simulated results show a similar change of magnetoresistance dependence with MW power as observed in the experimental data. There is some difference between simulated and experimental results in the position of the minima in the region (2).

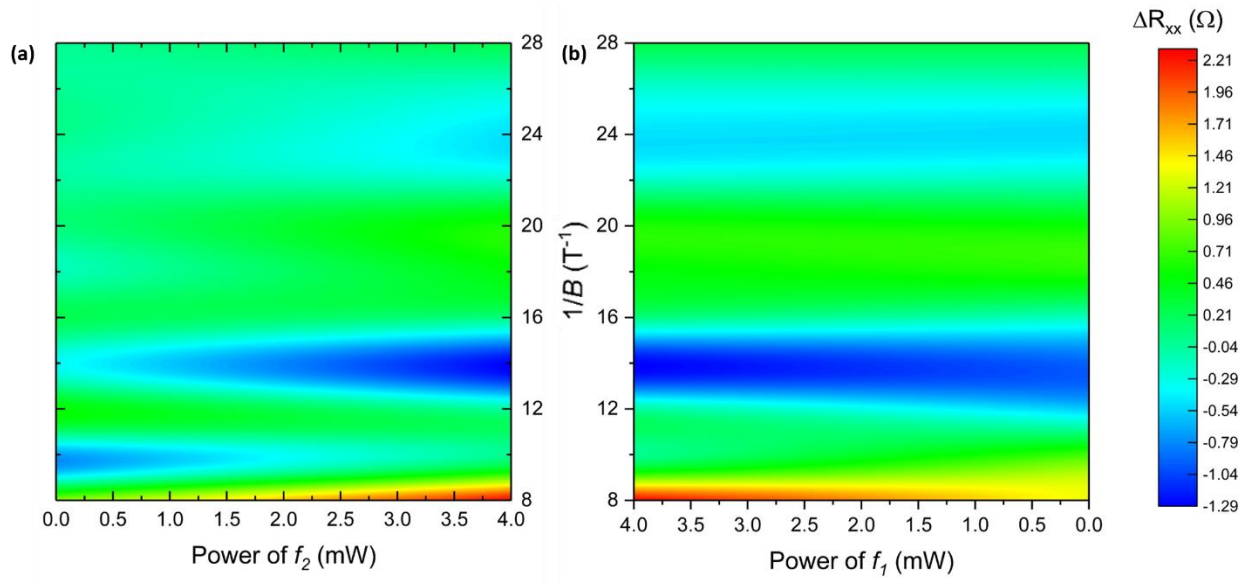

Figure 4.5 Diagonal resistance simulation with the change of MW power and the inverse magnetic field. While sweeping the magnetic field (a) MW power of f_2 was changed from $0\ mW$ to $4\ mW$ while using a fixed MW power of $4\ mW$ for f_1. (b) MW power of f_1 was changed from $4\ mW$ to $0\ mW$ while using a fixed MW power of $4\ mW$ for f_2. The color plot shows that the resistance variations at the low magnetic field happen only with the MW power change of the low monochromatic MW frequency, while the interference effect could be observed at high magnetic field regions (in preparation to be published).

Next, we removed the background resistance for the high and low-frequency components. First, we kept the MW power of f_1 at $4\ mW$ and changed the MW power of f_2 from $0\ mW$ to $4\ mW$. Then we fixed the MW power of f_2 and change the MW power of f_1 from $0\ mW$ to $4\ mW$. The corresponding results are in figure 4.5. The figure shows that at low magnetic fields such as $0.04\ T$, the change of the power of high-frequency MW does not affect the oscillatory behavior, but at high magnetic fields, we could observe a change of oscillatory diagonal resistance line shape with the high-frequency MW power increment. Here the magnetic field range is $0.03 - 0.125\ T$.

5 SUMMARY

Here we summarize the results and discuss the modifications to the experiments that could be done to further understand the bMIMO behavior on GaAs/Al GaAs 2D heterostructure systems.

5.1 Results

Dual radiation excitation of GaAs/AlGaAs 2DES in a perpendicular magnetic field changes the diagonal resistance (R_{xx}) lineshape in an exciting manner which codependent on many parameters. Diagonal magnetoresistance dependence on the magnetic field could be classified by splitting the magnetic field range into three main regions. The bichromatic MIMO response of the diagonal resistance, R_{xx} follows the low-frequency monochromatic response at low magnetic fields. At the intermediate magnetic field region, a shift from low-frequency MW response towards high-frequency MW is observed. It deviates towards the high-frequency monochromatic MW response as the magnetic field strength increases further.

A qualitative understanding of this bMIMO behavior could be achieved by developing a model, which takes into account an electron transition time between the LLs. A transverse magnetic field applied to a GaAs/AlGaAs 2DES produces LLs. The separation between those LLs ($\Delta E = \hbar\omega_c$) increases with the increment of the applied magnetic field. However, the photon energy of the MWs is fixed ($E = h\nu$) and does not depend on the magnetic field. It takes some time for the electron to get photoexcited to a higher LL from an incoming photon. Since the excitation from the low-frequency MW photon spans over fewer LLs than the excitation from the high-frequency MW photon, it is more probable for an electron to be excited by the low-frequency MW photon. Thus at a low magnetic field, the bMIMO follows the monochromatic low-frequency line shape. With an increase in the magnetic field strength, the LL separation increases. This lowers the LL span of a photoexcited electron for both MW frequencies. Hence, we could observe a

magnetic field region where the bMIMO line shape deviates from the low-frequency monochromatic response towards the high-frequency monochromatic response. At even higher magnetic fields, the LL separation increases beyond the low-frequency photon energy. In this case, we observe the high-frequency monochromatic MW lineshape characteristics in bMIMO response.

MIMOs are periodic with the inverse magnetic field. Plotting the corresponding node points (resonance and harmonic points) with the inverse magnetic field provides us a linear dependence with the slopes that are determined by the MW frequency. Those plots are known as the half-cycle plots. Identification of the node points could be made by looking at the line shape of the derivative of the diagonal resistance as it is more sensitive to the resistance variations. A small magnetic field was supplied in addition to the perpendicular magnetic field using a modulation coil around the sample. Here, we have used a two-Lock-in amplifier measuring system to obtain the derivative of the diagonal resistance. In the derivative of the diagonal resistance signal, resonance and harmonics are represented by the peaks of the lineshape. The half-cycle plots of bMIMOs show two slopes. One slope corresponding to the low-frequency monochromatic response, and the other to the high-frequency monochromatic response. Derivative of the diagonal resistance signal corresponds to the dual MW excitation also exhibit the previously observed magnetic field dependency. At the low magnetic field region, the half-cycle plot of bMIMO has a slope that corresponds to the low-frequency response, while at the high magnetic field, the bMIMO has a slope that corresponds to the high-frequency response. Additionally, it was observed that the bMIMO half-cycle plot follows only the slope that corresponds to either the high-frequency or low-frequency monochromatic MW response for our experiment.

It is evident that the MW power used for each frequency plays a major role for bMIMOs. We have used the line shapes and the half-cycle plots to get a clear picture of this behavior. Half-

cycle plots reveal that the magnetic field where bMIMO response starts to from one monochromatic frequency response to the other changes with the power used on each MW radiation used for the dual excitation. Using half-cycle plots has some limitations in identifying the correct magnetic field of bMIMO because only the data points at resonance and harmonics are used in this case. Although in some cases, the bMIMO line shape is the average of two monochromatic contributions, we have experimentally identified that the applied magnetic field and the MW powers significantly affect the bMIMO lineshape.

The radiation-driven electron orbital model could be modified to obtain the bMIMO behavior, and the line shape exhibits similar patterns as the experimental data. Experimentally the impurities of the sample, extra scattering channels, and other limitations of the measurement systems used damp the oscillatory behavior, especially at lower magnetic field regions. Those factors affecting the experiments and the corresponding experimental resistance lineshapes for bMIMOs are a little be different from the numerical results. But overall, the pattern of the lineshape change with the change of the low-frequency MW and high-frequency MW is similar in both the experimental and simulated results.

According to the model, the experimental result that shows the magnetic field dependence of bMIMOs is mainly due to the damping factors on the denominator of $A_{m(n)}^{\omega_1}$ and $A_{m(n)}^{\omega_2}$. When the magnetic field increases, especially beyond the resonance frequency condition, dampening takes place on that particular frequency. Since the low-frequency resonance condition is satisfied before the high-frequency condition with increasing magnetic field, the low-frequency response is dominant at small magnetic field, while the high-frequency response gives the main contribution at large magnetic field.

5.2 Further development

Previous experiments suggest that the effect of the bMIMO could depend on many parameters such as sample temperature, MW polarization angle, the current supplied to the sample, the mobility, and the density of the samples. Exploration of those matters with dual MW excitations could further characterize the behavior of bMIMOs. For example, the sample's density could be changed by using a back gate on GaAs/AlGaAs heterostructure. Hall bars could be designed to have different widths to examine the effect of sample size on bMIMOs.

Our model only deals with single-photon excitation, but experimentally, we could sometimes observe features in MIMO lineshape that suggests multiphoton excitations. New model improvements are needed to account for the multiphoton excitation of such systems.

Overall, our experiment and simulation provide a basic understanding of bMIMO behavior in GaAs/AlGaAs heterostructure 2DESs, which also opens potential applications of such setup in the field of MW detectors and temperature sensors.

REFERENCES

1. von Klitzing, K., *The quantized Hall effect.* Reviews of Modern Physics, 1986. **58**(3): p. 519-531.
2. Lei, X.L. and S.Y. Liu, *Magnetoresistance oscillations in two-dimensional electron systems under monochromatic and bichromatic radiations.* Applied Physics Letters, 2006. **89**(18): p. 182117.
3. Iñarrea, J. and G. Platero, *Theoretical Approach to Microwave-Radiation-Induced Zero-Resistance States in 2D Electron Systems.* Physical Review Letters, 2005. **94**(1): p. 016806.
4. Koulakov, A.A. and M.E. Raikh, *Classical model for the negative dc conductivity of ac-driven two-dimensional electrons near the cyclotron resonance.* Physical Review B, 2003. **68**(11): p. 115324.
5. Zudov, M.A., et al., *Bichromatic Microwave Photoresistance of a Two-Dimensional Electron System.* Physical Review Letters, 2006. **96**(23): p. 236804.
6. Bid, A. *Observation of neutral modes in the fractional quantum Hall regime*. 2011 [cited 2011 October 10-13]; The Condensed Matter Group at Harish-Chandra Research Institute organizes a workshop on Low Dimensional Quantum Systems during October 10-13, 2011.]. Available from: http://www.hri.res.in/~cmworksh/LDQS/talks/Aveek.pdf.
7. Mani, R.G., et al., *Zero-resistance states induced by electromagnetic-wave excitation in GaAs/AlGaAs heterostructures.* Nature, 2002. **420**(6916): p. 646-650.
8. Durst, A.C., et al., *Radiation-induced magnetoresistance oscillations in a 2D electron gas.* Physica E: Low-dimensional Systems and Nanostructures, 2003. **20**(1): p. 117-122.
9. Gunawardana, B., et al., *Millimeter wave radiation-induced magnetoresistance oscillations in the high quality GaAs/AlGaAs 2D electron system under bichromatic excitation.* Physical Review B, 2017. **95**(19): p. 195304.
10. Mani, R.G., et al., *Radiation-induced oscillatory magnetoresistance as a sensitive probe of the zero-field spin-splitting in high-mobility GaAs/AlGaAs devices.* Physical Review B, 2004. **69**(19): p. 193304.
11. Ezawa, Z.F., *Quantum Hall effects : field theoretical approach and related topics*. 2nd ed. ed. 2008: World Scientific.
12. Mollick, E., *Establishing Moore's law.* IEEE Annals of the History of Computing, 2006. **28**(3): p. 62-75.
13. Shik, A.Y., *Quantum wells : physics and electronics of two-dimensional systems.* 1997.
14. Ando, T., A.B. Fowler, and F. Stern, *Electronic properties of two-dimensional systems.* Reviews of Modern Physics, 1982. **54**(2): p. 437-672.
15. Sommer, W.T., *Liquid Helium as a Barrier to Electrons.* Physical Review Letters, 1964. **12**(11): p. 271-273.
16. Novoselov, K.S., et al., *Electric Field Effect in Atomically Thin Carbon Films.* Science, 2004. **306**(5696): p. 666-669.
17. Störmer, H.L., et al., *Two-dimensional electron gas at a semiconductor-semiconductor interface.* Solid State Communications, 1979. **29**(10): p. 705-709.
18. Levi, A.F.J., *Semiconductor band structure and heterostructures*, in *Essential Semiconductor Laser Device Physics*. 2018, Morgan & Claypool Publishers. p. 1-1-1-26.
19. Bussei, P., *Be diffusion in GaAs layers grown by MBE.* Acta Naturalia de l'Ateneo Parmense, 2002. **38**: p. 13-18.

20. Crawford, F.S., *Elementary derivation of the magnetic flux quantum.* American Journal of Physics, 1982. **50**(6): p. 514-516.
21. Samaraweera, R.L., *Effect of DC-Current and Microwave Excitations on Negative Magnetoresistance in GaAs/AlGaAs 2DES*. 2018: ScholarWorks @ Georgia State University.
22. Klitzing, K.v., G. Dorda, and M. Pepper, *New Method for High-Accuracy Determination of the Fine-Structure Constant Based on Quantized Hall Resistance.* Physical Review Letters, 1980. **45**(6): p. 494-497.
23. Wysokinski, K.I., *Introduction to quantum Hall effects.* Acta Physica Polonica A, 2001. **100**(3): p. 287-299.
24. Stoger, G., et al., *Shubnikov-de Haas oscillations and negative magnetoresistance under hot-electron conditions in Si/SiGe heterostructures.* Semiconductor Science and Technology, 1994. **9**(5S): p. 765-771.
25. Taboryski, R. and P.E. Lindelof, *Weak localisation and electron-electron interactions in modulation-doped GaAs/AlGaAs heterostructures.* Semiconductor Science and Technology, 1990. **5**(9): p. 933-946.
26. Zudov, M.A., et al., *Shubnikov--de Haas-like oscillations in millimeterwave photoconductivity in a high-mobility two-dimensional electron gas.* Physical Review B, 2001. **64**(20): p. 201311.
27. Zhang, S.-B., H.-Z. Lu, and S.-Q. Shen, *Edge states and integer quantum Hall effect in topological insulator thin films.* Scientific Reports, 2015. **5**(1): p. 13277.
28. *Edge-State Transport*, in *Perspectives in Quantum Hall Effects*. p. 109-159.
29. Tsui, D.C., H.L. Stormer, and A.C. Gossard, *Two-Dimensional Magnetotransport in the Extreme Quantum Limit.* Physical Review Letters, 1982. **48**(22): p. 1559-1562.
30. Stormer, H.L., *The fractional quantum hall effect (experiment).* Physica B+C, 1984. **126**(1): p. 250-253.
31. Lange, W.d., F.A.P. Blom, and J.H. Wolter, *Effective electron mass in GaAs/AlxGa1-xAs heterostructures under hydrostatic pressure.* Semiconductor Science and Technology, 1993. **8**(3): p. 341-343.
32. Mani, R.G., et al., *Zero-resistance states induced by electromagnetic-wave excitation in GaAs/AlGaAs heterostructures.* Nature, 2002. **420**(6916): p. 646-50.
33. Ramanayaka, A.N., R.G. Mani, and W. Wegscheider, *Microwave-induced electron heating in the regime of radiation-induced magnetoresistance oscillations.* Physical Review B, 2011. **83**(16): p. 165303.
34. Bogan, A., et al., *Microwave-induced resistance oscillations in tilted magnetic fields.* Physical Review B, 2012. **86**(23): p. 235305.
35. Ramanayaka, A.N., et al., *Effect of rotation of the polarization of linearly polarized microwaves on the radiation-induced magnetoresistance oscillations.* Physical Review B, 2012. **85**(20): p. 205315.
36. Ye, T., W. Wegscheider, and R.G. Mani, *Evolution of the linear-polarization-angle-dependence of the radiation-induced magnetoresistance-oscillations with microwave power.* Applied Physics Letters, 2014. **105**(19): p. 191609.
37. Zudov, M.A., et al., *Observation of microwave-induced resistance oscillations in a high-mobility two-dimensional hole gas in a strained Ge/SiGe quantum well.* Physical Review B, 2014. **89**(12): p. 125401.

38. Liu, H.-C., et al., *Frequency-dependent polarization-angle-phase-shift in the microwave-induced magnetoresistance oscillations.* Journal of Applied Physics, 2015. **117**(6): p. 064306.
39. Samaraweera, R.L., et al., *Mutual influence between current-induced giant magnetoresistance and radiation-induced magnetoresistance oscillations in the GaAs/AlGaAs 2DES.* Scientific Reports, 2017. **7**(1): p. 5074.
40. Nanayakkara, T.R., et al., *Electron heating induced by microwave photoexcitation in the GaAs/AlGaAs two-dimensional electron system.* Physical Review B, 2018. **98**(3): p. 035304.
41. Gunawardana, B., et al., *Behaviour of Bichromatic Microwave Induced Magnetoresistance Oscillations in the High Mobility GaAs/AlGaAs 2D electron System.* Journal of Physics: Conference Series, 2017. **864**: p. 012055.
42. Munasinghe, C.R., et al., *Electron heating induced by an ac-bias current in the regime of Shubnikov–de Haas oscillation in the high mobility GaAs/Al x Ga1−x As two-dimensional electron system.* Journal of Physics: Condensed Matter, 2018. **30**(31): p. 315701.
43. Ryzhii, V. and R. Suris, *Nonlinear effects in microwave photoconductivity of two-dimensional electron systems.* Journal of Physics: Condensed Matter, 2003. **15**(40): p. 6855-6869.
44. Lei, X.L. and S.Y. Liu, *Radiation-Induced Magnetoresistance Oscillation in a Two-Dimensional Electron Gas in Faraday Geometry.* Physical Review Letters, 2003. **91**(22): p. 226805.
45. Dmitriev, I.A., et al., *Mechanisms of the microwave photoconductivity in two-dimensional electron systems with mixed disorder.* Physical Review B, 2009. **80**(16): p. 165327.
46. Mikhailov, S.A., *Microwave-induced magnetotransport phenomena in two-dimensional electron systems: Importance of electrodynamic effects.* Physical Review B, 2004. **70**(16): p. 165311.
47. Lei, X.L. and S.Y. Liu, *Radiation-induced magnetotransport in high-mobility two-dimensional systems: Role of electron heating.* Physical Review B, 2005. **72**(7): p. 075345.
48. Dmitriev, I.A., et al., *Theory of microwave-induced oscillations in the magnetoconductivity of a two-dimensional electron gas.* Physical Review B, 2005. **71**(11): p. 115316.
49. Yar, A. and K. Sabeeh, *Radiation-assisted magnetotransport in two-dimensional electron gas systems: appearance of zero resistance states.* Journal of Physics: Condensed Matter, 2015. **27**(43): p. 435007.
50. Yip, S.K., *Extensions of Kohn's theorem.* Physical Review B, 1989. **40**(6): p. 3682-3684.
51. Ye, T., et al., *Comparative study of microwave radiation-induced magnetoresistive oscillations induced by circularly- and linearly- polarized photo-excitation.* Scientific Reports, 2015. **5**(1): p. 14880.
52. Brian, K.R., *Quantum Processes in Semiconductors*. Vol. Fifth edition. 2013, Oxford: OUP Oxford.
53. Lei, X.L., *Theoretical analysis of radiation-induced magnetoresistance oscillations in high-mobility two-dimensional electron systems.* Journal of Physics: Condensed Matter, 2004. **16**(23): p. 4045-4060.
54. Lei, X.L. and S.Y. Liu, *Multiple and virtual photon processes in radiation-induced magnetoresistance oscillations in two-dimensional electron systems.* Applied Physics Letters, 2006. **88**(21): p. 212109.

55. Kerner, E.H., *NOTE ON THE FORCED AND DAMPED OSCILLATOR IN QUANTUM MECHANICS*. Canadian Journal of Physics, 1958. **36**(3): p. 371-377.
56. Park, K., *Radiation-induced zero-resistance state at low magnetic fields and near half-filling of the lowest Landau level*. Physical Review B, 2004. **69**(20): p. 201301.
57. Brian, K.R., *Quantum Processes in Semiconductors*. Vol. 4th ed. 1999, Oxford: OUP Oxford.